BearWorks

Summer 2019

Structure and Properties of ZnO-ZnS Heterostructures

Sanchali Das
Missouri State University, Sanchali026@live.missouristate.edu

STRUCTURE AND PROPERTIES OF ZnO-ZnS HETEROSTRUCTURES

A Master's Thesis

Presented to

The Graduate College of

Missouri State University

In Partial Fulfillment

Of the Requirements for the Degree

Master of Science, Material Science

By

Sanchali Das

August 2019

STRUCTURE AND PROPERTIES OF ZnO-ZnS HETEROSTRUCTURES

Physics, Astronomy and Material Science

Missouri State University, August 2019

Master of Science

Sanchali Das

ABSTRACT

Heterostructures consisting of at least two layers of dissimilar materials have always been well studied due to potential applications in nano-electronic and optoelectronic devices. In this study, I have investigated the structural and physical properties of zinc oxide -zinc sulfide (ZnO-ZnS) based heterostructures of thin films and core-shell nanoparticles. Pulsed laser deposition technique was employed to grow ZnO thin film on sapphire substrate. ZnO-ZnS heterostructures were obtained using hydrothermal synthesis where thiourea has served as a precursor solution for the source of sulfur. X-ray diffraction analysis on the parent and the sulfidized samples gives the information about the crystallinity and the phase of the heterostructures. Scanning electron microscope analysis provides the morphological and constituent elemental information of the heterostructures. Variation of the time and temperature of the sulfidation can alter the structure and properties of the heterostructures. At a given temperature, the amount of sulfidation depends on the exposure time on the sulfur rich environment. The more the availability of sulfur ions due to thiourea decomposition, the more is the growth of ZnS at the ZnO-ZnS interface. Raman spectroscopy gives the vibrational states present in the both parent and synthesized heterostructures while photoluminescence analysis provides information about optical band gap and defect states that are present in the heterostructures.

KEYWORDS: heterostructures, optoelectronics, crystallinity, vibrational states, band gap, photoluminescence, hydrothermal synthesis

STRUCTURE AND PROPERTIES OF ZnO-ZnS HETEROSTRUCTURES

By

Sanchali Das

A Master's Thesis
Submitted to the Graduate College
Of Missouri State University
In Partial Fulfillment of the Requirements
For the Degree of Master of Science, Material Science

August 2019

Approved:

Kartik C Ghosh, Ph.D., Thesis Committee Chair

David Cornelison, Ph.D., Committee Member

Ridwan Sakidja, Ph.D., Committee Member

Tiglet Besara, Ph.D., Committee Member

Julie Masterson, Ph.D., Dean of the Graduate College

In the interest of academic freedom and the principle of free speech, approval of this thesis indicates the format is acceptable and meets the academic criteria for the discipline as determined by the faculty that constitute the thesis committee. The content and views expressed in this thesis are those of the student-scholar and are not endorsed by Missouri State University, its Graduate College, or its employees.

ACKNOWLEDGEMENTS

TABLE OF CONTENTS

LIST OF TABLES

LIST OF FIGURES

INTRODUCTION

A heterostructure is a sandwich structure consisting of two dissimilar materials. Generally, semiconductor heterostructures made of two dissimilar semiconductors having different band gap values can create unique structural and electrical properties.[1] The difference in the band gap enables spatial confinement of injected electrons and holes. The difference in the refractive index between two dissimilar semiconductors can aid forming waveguide.[2] Heterostructures have interesting properties like confined carrier motion that enhances carrier mobility in doped semiconductor. Heterostructures have applications in several devices like laser diode, light emitting diode, solar cell, optical detectors, high electron mobility transistors (HEMTS).[3]

Most popular semiconductors exploit III-V and IV-VI compounds with similar crystal structures and less mismatched lattice constant.[1] Researchers have studied GaAs and $Al_xGa_{1-x}As$ extensively along with other heterostructures.[4] A close lattice matching is necessary for growth of epitaxial layers of heterostructures for prevention of the carrier recombination at the heterojunction interface. As there is growing interest in the field of thin film and nanotechnology, ultrathin multilayer heterostructures are being studied more extensively. Quantum confinement is one of the intriguing phenomena in the heterostructure when narrow energy band gap layer becomes atomically thin such as few tens of nanometers or even less than that.[5] Especially, this becomes more pronounced when the layer or the film dimension becomes comparable with De-Broglie wavelength. This ultrathin heterostructures are known as superlattices. As the size of materials approaches nanoscale range (less than 100 nm) surface properties become more prominent compared to the bulk properties. Same goes true for ultra-thin

1

or nanostructure heterojunction. High surface to volume ratio of the nanoscale materials gives rise to unique novel properties.

Prevalent methods of epitaxial growth mechanism such as molecular beam epitaxy (MBE) and Metal organic chemical vapor deposition (MOCVD) have enabled fabrication of wide variety of thin layers of semiconductor compounds on various single crystalline substrates.[6] These heterostructures based devices can be classified into two groups: Heterojunction and Quantum Well.

Heterojunctions are comprised of two layers A and B, and electrons or holes exist between the interface layers. The quantum well can be represented in the form of ABA where the central layer may confine charge carriers if the system is doped. For both heterojunction and quantum well, charge carriers are trapped in two dimensions. High electron mobility and strong electron-electron interaction are the result of electron confinement. The restriction of the charge carriers (electron, hole or exciton) in the direction normal to the film or layer can be considered carrier confinement in one dimension. For thin films, well can be considered as deep infinite square well. For semiconductor heterojunction the potential wells are finite and rectangular in profile.

Superlattices are comprised of multiple periodic array of semiconducting compounds in the form of ABAB layers.[6] Multiple quantum well of composition ABAB…contains wide barriers such that carriers are confined in separate well. While the characteristics of a superlattice can be approximated by Kronig-Penny model where role of the interface is very important for the electronic properties.

Most of the active photonic devices utilize III-V semiconductor heterostructures where the optical properties are very important. Some of the properties like spontaneous emission,

absorption spectra, and refractive index, despite having been studied for decades by researchers, it has remained hard to approach device modelling.[7] It is necessary to study the microscopic details of light matter interaction in III-V semiconductor for both bulk and nanomaterial for a multilayer device, especially how carrier injection is utilized for doped or undoped layers. Previous researchers reported that for direct band gap semiconductors like GaAs or InP Kane model is being used for approximation. It considers conduction band (Γ valley) with the heavy-hole, light hole and split-off valence band. X and L valleys play an important role to determine electron Fermi level and intra-band absorption co-efficient. After the electron states and carrier distribution of those are determined, the rate of radiative transition is calculated using perturbation theory.[7] For the calculation of the first order process six types of direct radiative recombination are considered. For second order process, scattering mechanisms were incorporated approximating three parabolic sub-band valence band and non-parabolic multivalley conduction band.

ZnO and ZnS are popular wide band-gap group II-VI semiconductors used for fabricating optoelectronic and photonic devices. Heterostructures of wurtzite ZnO (band gap 3.37ev) and wurtzite ZnS ($E_G \sim 3.72ev$) or zinc-blende ZnS ($E_G \sim 3.7ev$)[8] have applications in ultraviolet laser and photovoltaic detectors.

Yan *et al.*[8] reported synthesis of biaxial ZnO/ZnS nano heterostructure which has been challenging till this date. They investigated growth and structure of 1D heterostructure comprising of II-VI semiconductors. They also studied excitonic properties of these structures by employing cathodoluminescence spectroscopy. They synthesized hetero-crystalline ZnS /single crystalline ZnO based biaxial nanobelts by thermal evaporation method where gold is used as catalyst. The TEM image revealed uniform interface between the upper ZnS and lower ZnO

fragment. The individual diameters were reported to be 40nm and 30nm in individual ZnS and ZnO domain. They reported that the ZnO fragment was wurtzite in structure and ZnS portion comprised of hetero-crystalline superlattice structure of alternative zinc blende (ZB) and wurtzite (WZ) ZnS sections. For investigation of the optical properties of the heterostructure, cathodoluminescence (CL) was studied on the sample. A broad emission spectrum was reported around $\sim$ 535 nm and a weak UV emission band was centered around$\sim$ 345 or ~385 nm. This result was consistent with the reported morphology of ZnS/ZnO nano heterostructure.

Heterostructure device consisting of two dissimilar materials with unique structural and optoelectronic properties can exhibit enhanced performance such as emission efficiency or distinct luminescence properties. ZnS-In based heterostructure was reported to show enhanced emission efficiency, SnO_2-ZnO heterostructure exhibited unique luminescence properties.[9] Three dimensional ZnO/Si based heterojunction improves the efficiency for solar water splitting. Tian *et al.*[9] previously reported ZnS nanobelt based UV-light sensors which, however, shows weak photocurrent and poor stability. ZnO nanostructure based UV photodetectors exhibits poor photocurrent stability and slow responsivity mostly due to internal defects like oxygen vacancies or zinc interstitials.[9] However, it has been established that highly crystalline ZnS based photodetectors have faster response and speed while ZnO with good contacts can generate large photocurrent. By combining these unique properties, they fabricated hybrid ZnO-ZnS based photodetector which is potentially promising for UV-light sensors. This fabricated device has shown fast response speed, tunable spectral selectivity and enhanced photoresponsivity. The ZnO-ZnS heterostructure have shown biphase mixture of wurtzite ZnO and wurtzite ZnS with low level impurity. Two luminescence spectra have been observed at $\sim$ 396nm and ~530 nm for ZnO-ZnS hybrid structure. The green emission spectra around 530 nm resulted from ZnO

nanorod within the hybrid structure. According to this paper, the linear I-V characteristic curve was reported which indicates good Ohmic contacts between the electrodes and the film. The device was illuminated with light sources of different wavelength of 300, 320,350,380 nm. The increase in photocurrent was reported for the excitation wavelength below 380nm. This is due to increased number of electron-hole pairs when excitation energy is greater than the band gap of the ZnO-ZnS heterostructure.

Lu *et al.*[3] reported vertically aligned ZnO-ZnS heterojunction nanowires, synthesized by thermal evaporation in presence of residual oxygen. These were used to convert mechanical energy to electrical energy. Vertical ZnS nanowire arrays were synthesized by selective etching ZnO-ZnS nanowire arrays. Wurtzite structure of both ZnO and ZnS were being reported. TEM images have shown epitaxial growth of ZnO above ZnS nanowires at the interface. Large lattice mismatch between ZnO and ZnS can result into thin intermediate thin layer in between. Both TEM and EDS results have confirmed ZnO-ZnS heterojunction nanowire array. The piezoelectric property was examined by using atomic force microscopy (AFM).[3] CL measurement of ZnO-ZnS array has shown emission around 509 nm. For this paper, the goal was to synthesize ZnO-ZnS heterostructure and study the structural and optical properties of the nano-heterostructure. ZnO being a wide direct band gap semiconductor with high exciton binding energy (60 mev) has good thermal and chemical stability.[10] ZnO has been well studied for divergent applications in different fields such as piezoelectric material, UV light emitting diode, gas sensing, transparent conductive oxide (TCO) layer in thin film based solar cell, and transducer.[10] Several studies have proved the presence of defect sites such as oxygen vacancies, oxygen interstitial, and zinc interstitial and so on which gives rise to the defect related band in photoluminescence spectrum. Zinc oxide crystallite has two different crystal structure i) wurtzite

and ii) zinc blende.[11] Wurtzite is the most stable structure where each anion is bonded with four cations at the corner of a tetrahedron.[11] Figure 1 represents the structure of wurtzite.
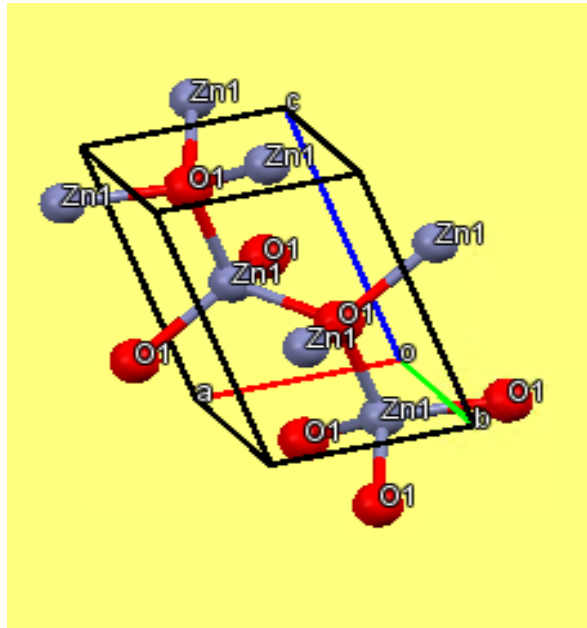
Figure 1: Unit cell of wurtzite ZnO

Zinc sulfide (ZnS) is a popular wide band gap (3.7ev) II-VI semiconductor material for wide variety of application such as light emitting diode, optical coating, electroluminescent devices, heterojunction solar cell[12] and so on. Effective phosphor material also fabricated using ZnS thin films doped with transition metal.[13] Zinc sulfide exists in two different polymorphs. i) Zincblende (sphalerite) and ii) wurtzite. In zinc blende structure, the sulfur atoms occupy the fcc sites where zinc atoms occupy half of the tetrahedral sites. This structure is also considered as two inter-twined fcc lattice corresponding to each sulfur and zinc with the origin displaced at half of the body diagonal. The reported lattice parameter is a= 0.541 nm. In wurtzite structure the sulfur ions arrange themselves in HCP array and half of the tetrahedral sites are occupied by zinc

ions. In this study, thin film heterostructure of ZnO/ZnS was fabricated using pulse laser deposition (PLD) technique and hydrothermal method. Also, we synthesized sulfur doped nano heterostructure of ZnO/ZnS core-shell nanoparticles. Figures 2 and 3 represent the unit cell structure of zinc-blende and wurtzite ZnS.
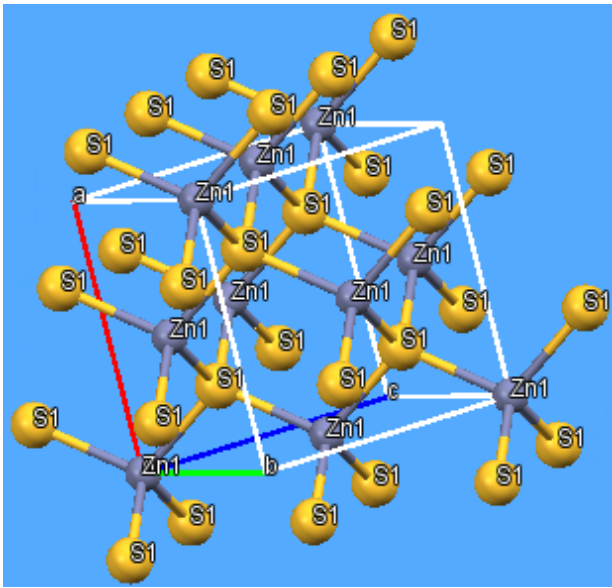
Figure 2: Unit cell of zinc blende ZnS   Figure 3: Unit cell of wurtzite ZnS
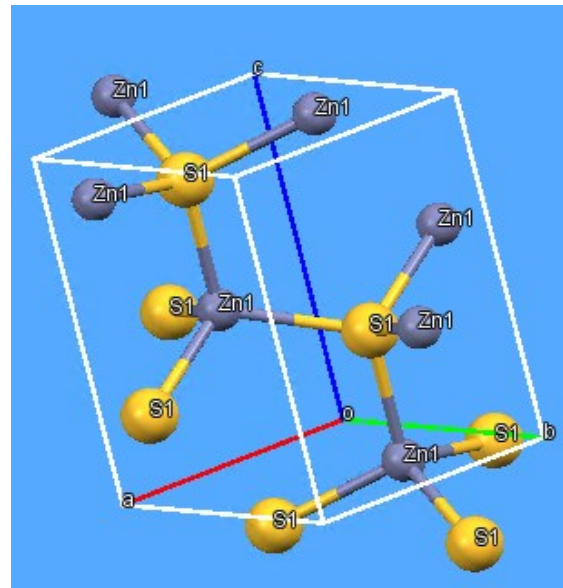
The structural properties were studied using XRD, SEM and EDS. Understanding the structural and physical properties of ZnO-ZnS based heterostructures can lead to develop efficient optoelectronic devices. Figures 4 and 5 represent the schematics of ZnO-ZnS thin film and CSNP based heterostructure.

Very few studies have been done on the sulfidation of ZnO thin film and development of the ZnO/ZnS heterostructures. Zhang *et al.*[14] reported sulfidation of ZnO thin film by annealing at 500°C in H_2S gas mixture. According to their study, H_2S gas is highly reactive and easily controllable for sulfidation of ZnO thin film compared to sulfur vapor. However, the underlying

mechanism of sulfidation or the physics behind it, is not very clear from their study. Bezverkhyy et al.[15]conducted sulfidation of pure and Cu-doped ZnO nanoparticle at 250 and 350°C using gaseous H_2S. The resulted structure was studied through transmission electron microscopy (TEM) and in situ synchrotron XRD. Partial sulfidation of ZnO with H_2S has resulted formation of cavities at the ZnO/ZnS interface which confirmed sulfidation of ZnO accompanied through outward growth of ZnS.
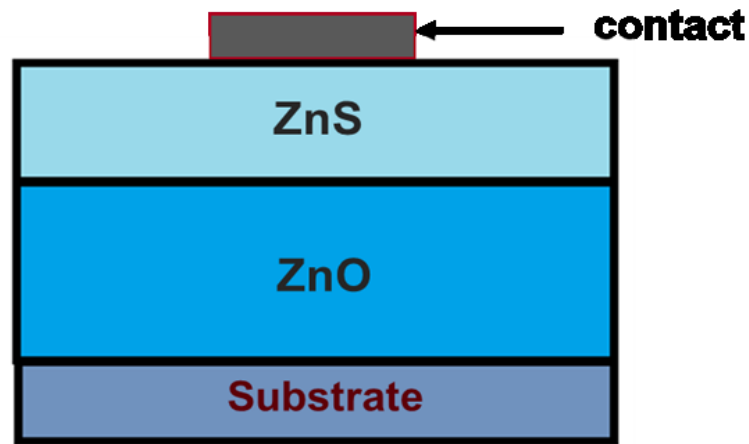
Figure 4: ZnO-ZnS thin film heterostructure
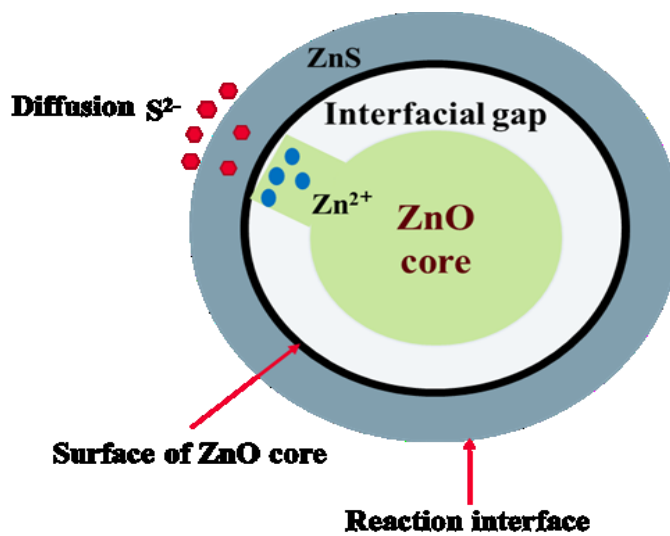
Figure 5: ZnO-ZnS core-shell heterostructure

This phenomenon is known as Kirkendall effect which proved Zn^{2+} and O^{2-} ions migrated to the external ZnS/ H_2S interface. For Cu-doped ZnO inward growth process was observed which depicts diffusion of S^{2-} anions from external H_2S gaseous phase to internal ZnO/ZnS interface where exchange of anions take place. In our experiment, exchange of anions in ZnO happens from thermal decomposition of aqueous solution of thiourea which serves as a source of sulfur. In addition, with XRD, Raman, PL and SEM analysis, TEM micrograph needs to be analyzed to observe formation of voids at the interface of ZnO/ZnS nanostructure. The diffusion mechanism is strongly dependent on activation temperature and time. Figure 6 represents migration of atoms through lattice via vacancy formation.
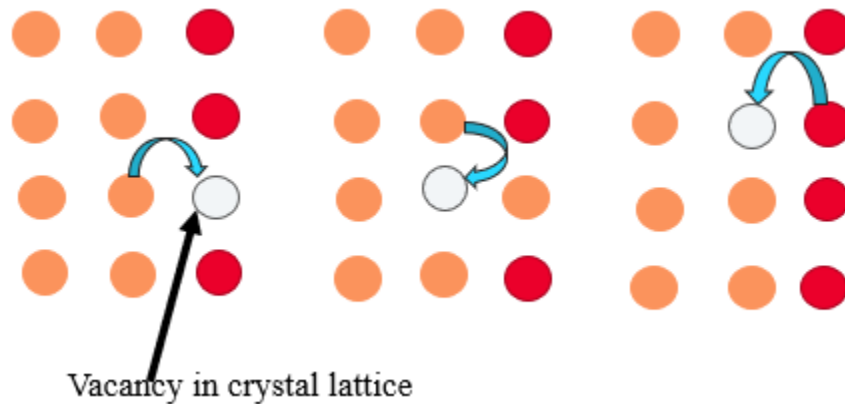
Figure 6: Migration of atoms via vacancies in lattice

Proper temperature can accelerate the migration of anions and cations through crystal structure. Hence vacancy related defect in parent crystal structure will be helpful for faster diffusion of S^{2-} anions to be exchanged with O^{2-}.

STRUCTURAL AND OPTICAL PROPERTIES OF HETEROSTRUCTURES OF ZnO-ZnS THIN FILMS

Abstract

C-axis oriented ZnO-ZnS thin film heterostructures have been synthesized by sulfidation of the pulsed laser deposited ZnO thin films using thiourea solution in hydrothermal synthesis. The PLD grown ZnO films were sulfidized at 180°C for varying amounts of time. The parent ZnO and the sulfidized films were characterized by x-ray diffraction, scanning electron microscopy (SEM) and energy dispersive electron spectroscopy (EDS). Optical properties were studied through Raman and photoluminescence spectroscopy. It turns out through structural analysis that crystallinity and preferred C-axis orientation decreases with initial sulfidation and regain with sulfidation time. We also found that porosity of the film enhances the exchange of oxygen to sulfur ion. PL spectroscopy data provide information about the defect related states present in the band gap of pure ZnO and the sulfidized films. More exposure time in the sulfur environment showed better and prominent sulfidation retaining the wurtzite crystal structure. Raman spectroscopy provides information about the vibrational modes present in both parent and the sulfidized films.

Introduction

ZnS being a high direct band gap semiconductor (3.54ev-cubic/ 3.91ev-WZ)[16] has potential applications in numerous optoelectronic devices such as light emitting diode, solar cell[14], electronic displays, and sensors.[17] Several synthesis methods are popular to fabricate ZnS

thin films such as chemical bath deposition (CBD),sol-gel, chemical vapor deposition (CVD), magnetron sputtering, and molecular beam epitaxy.[14] Very few papers reported synthesis of ZnS thin films by PLD method using a ZnS target. In most of the reported papers, ZnS thin film has been deposited on preferred substrate by magnetron sputtering method using a compound sputtering target.[14] Some other papers reported CBD method as large area and cost-effective production of ZnS thin film in relatively low temperature. But in general, the CBD grown films are either amorphous or not very crystalline in nature.[18] Therefore , we have approached a different path to synthesis ZnS thin film using the combination of pulse laser deposition(PLD) and hydrothermal synthesis. In this paper, ZnO-ZnS thin films are fabricated by sulfidation of ZnO thin films prepared by PLD. Even though sulfidation of ZnO thin film has been reported previously by Zhang *et al.*[14], their methodology was different. According to that paper, ZnO thin films were deposited by reactive sputtering from a Zinc (Zn) target. These ZnO films were sulfidized at 500°C in sulfur vapor. Influence of RF power and effect of sulfidation temperature were studied to understand the properties of ZnS thin films. Another research group reported annealing of ZnO thin films prepared by spray pyrolysis method in presence of sulfur powder at 450°C.[19]

In my experiment, I deposited ZnO thin film on sapphire substrate by PLD method and the sulfidation reaction was carried out by hydrothermal synthesis using a precursor solution of thiourea which acts as a source of sulfur. Good quality ZnO films were developed via PLD which resulted in moderate deposition rate of the species and appropriate temperature was helpful for thermal mobility and adhesion of species on the substrate. The oxygen in the metal oxide films were replaced by sulfur by diffusion mechanism of the sulfur atoms. After the growth, the structural and optical properties of the resultant ZnS films were analyzed.

Experimental Methods

Figure 7 represents flow chart diagram of synthesis process of ZnO -ZnS thin film heterostructure.
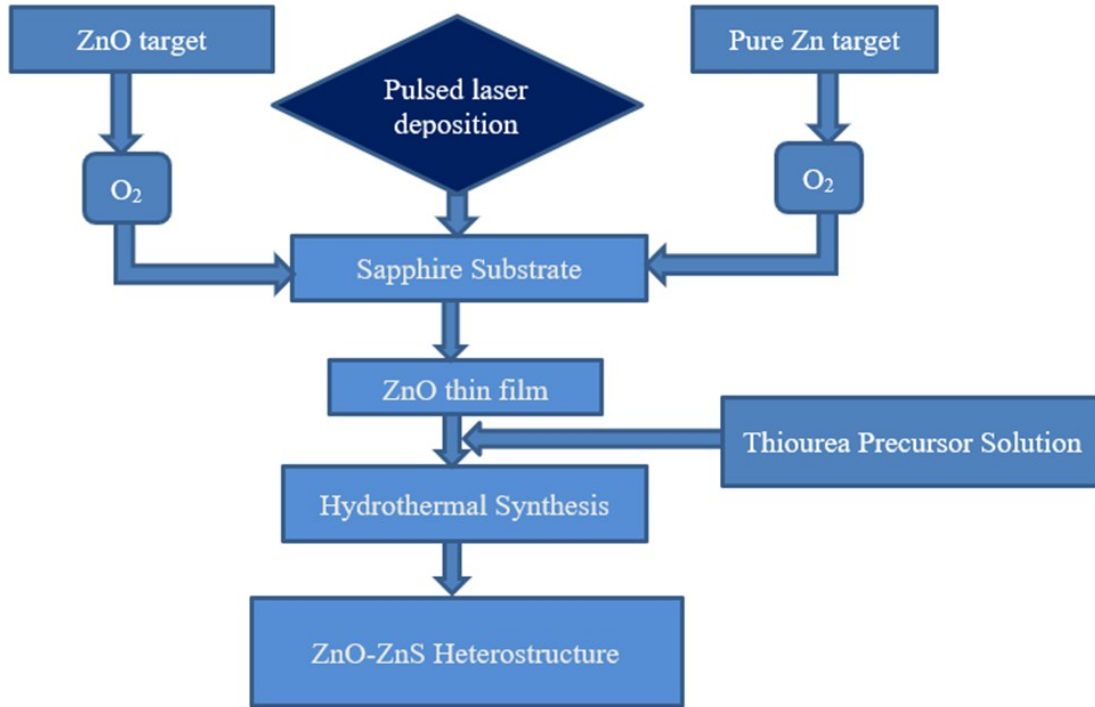
Figure 7: Flow chart diagram of the synthesis of ZnO-ZnS thin film heterostructures.

C-axis oriented porous ZnO films were grown on single crystal (0001) sapphire substrates (α-Al_2O_3) by PLD. Both ceramic ZnO and metallic zinc target were used for laser ablation. The ceramic ZnO target (diameter 1.00"×0.25"thick) was prepared by conventional pressed method at 100 Mpa pressure using 99.99% pure ZnO nano powder which was sintered at 1300°C in air. To carry out the deposition first the stainless-steel vacuum chamber was evacuated to the base pressure of 6.5×10^{-5} mbar using a turbo molecular pump. A solid-state pulsed Nd: YAG laser (wavelength 266nm) was focused on the rotating Zn or ZnO target to ablate the species. During

deposition the chamber was filled up with high purity oxygen gas with varying pressure of 4×10^{-2} to 4×10^{-1} mbar. The target to substrate distance was kept at 35mm and deposition temperature was maintained at 600°C to enhance the mobility of the deposited species on the substrate. The laser energy density was 2.54J/cm^2. 500 laser shots were used to pre-clean the target and 20,000 shots were given for laser ablation for the duration of 45 minutes (repetition rate 10Hz, Q-switch delay-5μs). After deposition, ZnO films were annealed in oxygen atmosphere of 1.1×10^{-1} mbar pressure at 600°C for an hour. The average film thickness measured after annealing by Veeco, Dektak was around 140nm.

The as-deposited porous ZnO films were sulfidized by hydrothermal synthesis where thiourea dissolved in DI water served as precursor solution. Different As grown ZnO thin films were immersed in .1M thiourea aqueous solution (prepared by dissolving 133mg thiourea in 17.5 ml DI water) inside an autoclave which was heated at 180°C for 16-hour, 4-hour and 1-hour respectively. After sulfidation, the autoclave was cooled down to room temperature and the sulfidized films were thoroughly rinsed with de-ionized water.

The sulfidation mechanism inside the autoclave took place after the thermal decomposition of thiourea [$CS(NH_2)_2$] in aqueous solution. A possible reaction could be as below.

$H_2O \rightarrow H^+ + OH^-$

$OH^- + CS(NH_2)_2 \rightarrow SH^- + CO(NH_2)_2$ (urea)
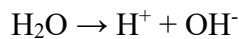
SH- ion could serve as source of S2- ions which can exchange with O^{2-} in ZnO.

In general, the reaction can be represented as the following steps below.

$H_2O + CS(NH_2)_2 \rightarrow H_2S + CO(NH_2)_2$ (urea)

$ZnO + H_2S \rightarrow ZnS + H_2O$
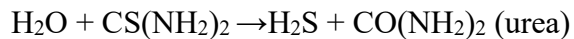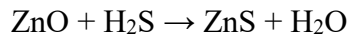
The crystallinity and the phase of the as-deposited ZnO films and the sulfidized samples were characterized by x-ray diffractometer (Bruker AXS D8) equipped with high-resolution detector using Cu-Kα source with wavelength of 1. 5406Å.The operating voltage and current were 40 kv and 40 mA, respectively. The θ-2θ scan was performed from 20° to 80° after optimization of ϕ and Z-axis scan. The data were analyzed using Origin pro 8.5.

The surface morphology of the as-deposited porous ZnO films and the ZnO-ZnS heterostructure films were studied through a scanning electron microscope (FEI Quanta 200). An energy dispersive x-ray spectroscopy detector (EDS) equipped within the same system was used for elemental analysis of the samples. SEM gives the information about the size and shape of the material. The microscope was operated at 10KV accelerating voltage while the working distance was fixed at 10 mm, measured spot size was 3.0. The EDS acquisition time was 120sec and performed by selecting a rectangular area on the sample. Several spots were studied to get better statistical measurement of the sample. Conductive gold or carbon coating was sputtered on the samples before performing the SEM-EDS measurement because the sapphire substrate is an insulating material which can result into charge build up on the sample surface that can create band bending resulting in distortion in image.

The Raman spectroscopy technique was employed to probe the information about vibrational energy states present in the crystal. The basic principle of Raman spectroscopy is based on inelastic scattering of incident excitation through the interaction of atomic and molecular vibration of the sample. As the intensity of anti-stokes scattering is 100 times less than stokes-scattering, stokes scattering was studied. All ZnO-ZnS heterostructures were characterized using 532nm green laser by Horiba Labram HR Raman PL system.10x objective

lens was used for initial focusing. 50x lens was helpful to determine more localized spot. For photoluminescence spectroscopy, the samples were irradiated with 325 nm He-Cd laser source at room temperature. Excitation energy was above the band gap of the material. The samples were placed on a metal bar of tungsten carbide which contributes minimum background signal. The 15x NUV-lens was used for focusing on the localized spot and measurements were taken at multiple spots. Beam splitter UV splits the scattered light from the sample according to the wavelength. The scan was taken in the range of 350-750 nm while acquisition time was 20 seconds, and 20 scans were taken in average in that wavelength range. Both Raman and PL spectroscopy data were analyzed using origin pro 8 software.

Results and Discussion

Figure 8 represents XRD patterns of as grown and annealed porous ZnO thin films. Several samples were synthesized via pulsed laser deposition. A strong diffraction is observed at $2\theta= \sim34.5°$ which corresponds to hexagonal wurtzite phase (002) and a weak diffraction peak appears at $2\theta= \sim72.5°$ which corresponds to (004) phase. It is evident that all ZnO films have preferred orientation along the C-axis perpendicular to the sapphire (0001) substrate because of lowest surface free energy along that direction.[20] Diffraction peaks of two parent ZnO films are represented in Figure 8. The crystalline quality can be interpreted from the full width half-maximum and intensity of ZnO (002) peak. Table 1 represents the values of FWHM for two different parent films . Smaller value of FWHM indicates better crystalline qualities of the synthesized film. It also indicates higher crystallite size of the PLD grown films. As calculated in Table 1, the narrow FWHM and higher intensity of XRD peaks depict better crystalline quality of the films annealed in O_2 atmosphere. The crystallite size can be calculated using Debye-

Scherrer formula as given below.
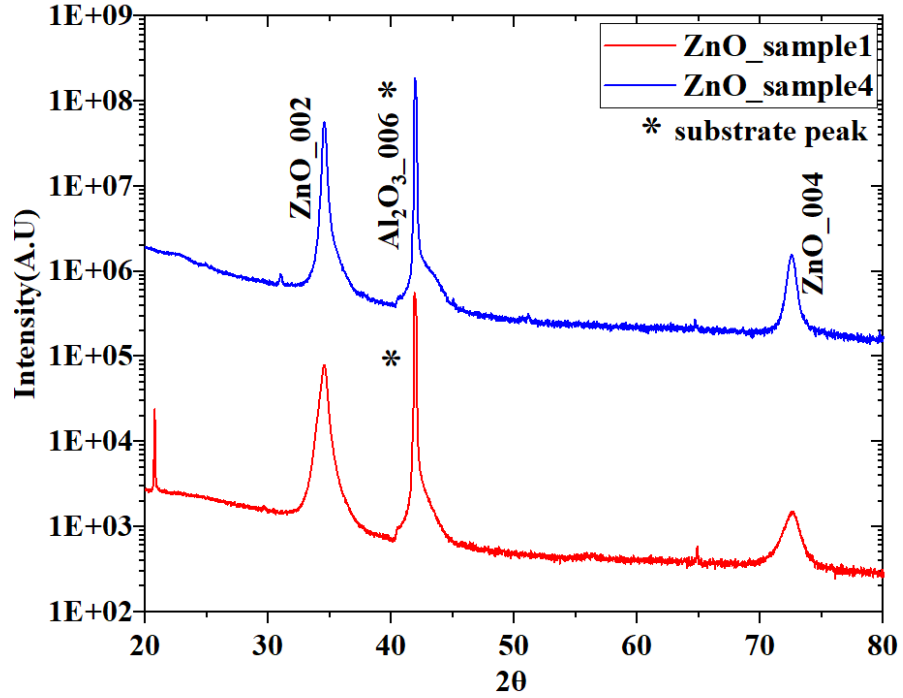
Figure 8: XRD data of porous ZnO parent

Table 1: FWHM and crystallite size calculation for porous ZnO parent films

ZnO Parent Sample	K	FWHM	λ(Å)	Θ(rad)	cosΘ(rad)	ß(rad)	L(nm)	h	k	L
1	0.9	0.64917	1.5406	0.3016	0.954	0.011330154	12.82	0	0	2
4	0.9	0.8302	1.5406	0.298	0.956	0.014489723	8.7	0	0	2

From the above Table, I observed higher crystallite size of sample 1 compared to sample 4 which depicts higher crystallite growth of parent sample 1 after annealing in oxygen atmosphere.

16

This might have resulted from variation of the background oxygen pressure during synthesis and growth of the parent ZnO films. The .Cif file gives confirmation of the crystallographic orientation in figure 9.
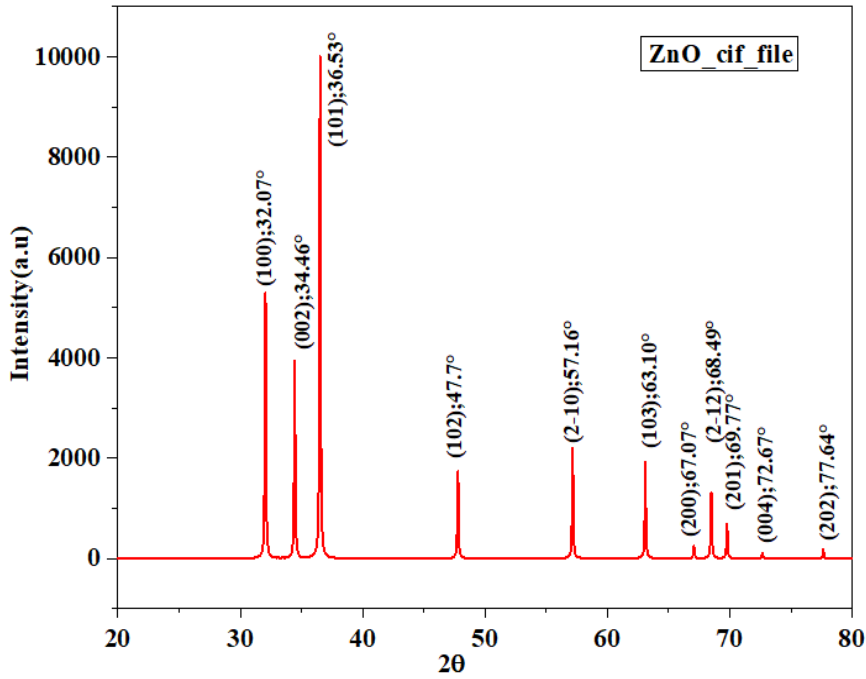
Figure 9: Cif data of wurtzite ZnO

$$particle\ size(\tau)\ =\ \frac{k\lambda}{\beta cos\theta}\ \text{where}$$

τ = mean size of the ordered crystalline domain

k = dimensionless shape factor 0.9

β = line broadening at half of the maximum intensity (FWHM) in radian

θ = Bragg angle

Table 2 shows the lattice parameters of ZnO films.

17

Table 2: Lattice parameter of the porous ZnO parent films

ZnO Parent Sample	$2\Theta(°)$	$d_{hkl}(Å)$	hkl	$a(Å)$	$c(Å)$
1	35	2.5932	0 0 2	3.18	5.186
7	34	2.6234	0 0 2	3.219	5.247

From Table 2 ,it can be seen that the lattice parameters got matched well with the theoretical standard values of hexagonal ZnO (a= 3.1249Å and c= 5.20 6Å).[21] Sulfidation was performed on different parent ZnO film for variable amount of time i.e 16 hours ,4 hours and 1 hour. Figure 10: a) and b) shows the XRD of the sample which was sulfidized for 16 hours and the .cif file for wurtzite ZnS respectively. From Figure 10, a significant diffraction peak at $2\theta = 28.7°$ which corresponds to hexagonal wurtzite phase (002) of ZnS was observed. Another small peak appears at $2\theta = 30.8°$ which might be an intermediate phase between ZnO and ZnS. It can be termed as $ZnO_{1-x}S_x$ (zinc oxy-sulfide) or it could be possibly ZnS (101) phase. Figure 11 represents XRD of two sulfidized ZnO films which were sulfidized for 4 hours for two different porous ZnO parent samples. From Figure 11, I observed that after 4 hours of sulfidation ZnO has partially converted to ZnS. Diffraction peaks at $2\theta = 28.7°$ (ZnS 002) and the intermediate peak at $2\theta = 30.8°$ matches with the previous result. From the plot, it is pronounced that the intensity of the diffraction peak at $2\theta = 28.7°$ is less for 4 hours sulfidation compared to 16 hours sulfidation. This demonstrates that after 16 hours sulfidation most of the ZnO film has converted to hexagonal ZnS. Figure 12, represents the XRD of the sulfidized ZnO peak that is 1 hour sulfidized and Figure 13, represents the overlapping plot of XRD of the sulfidized samples for

different amount of time.

(a)
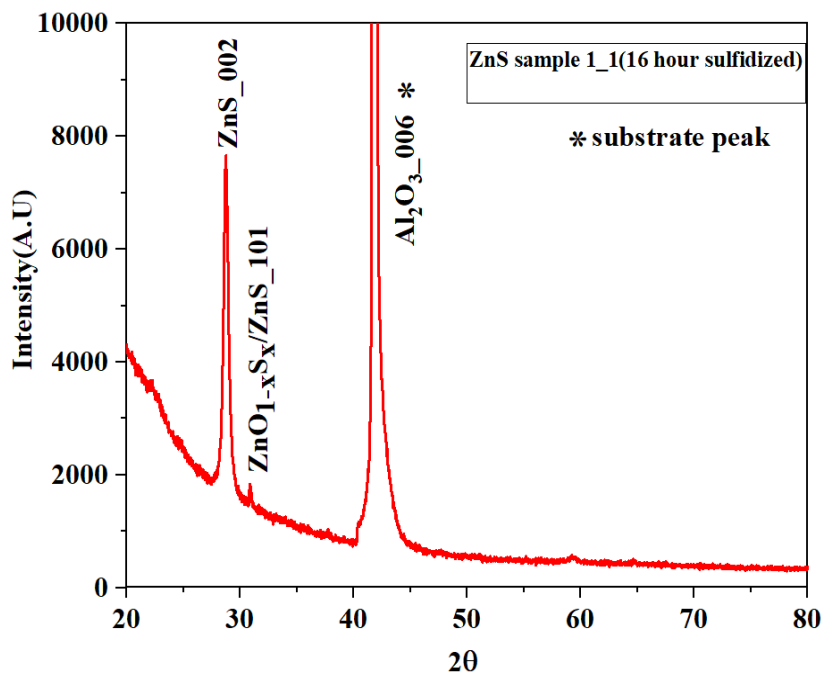
(b)
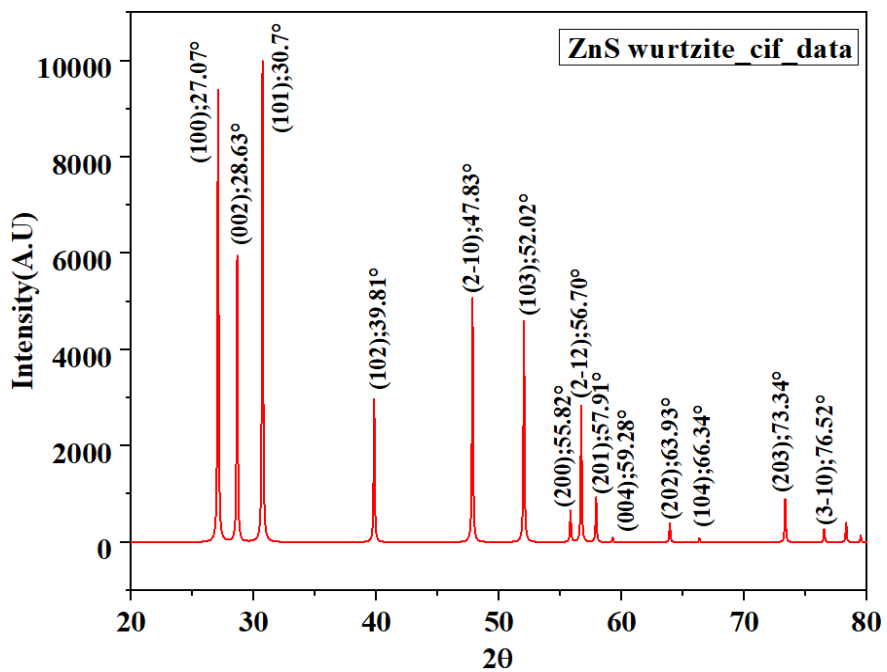
Figure 10: a) XRD of sulfidized sample (16hr) b) cif file of ZnS

Two different sulfidized porous ZnO parent films which were sulfidized for 4 hours, better crystallinity was achieved for the sample that was annealed in low oxygen atmosphere during the synthesis of parent ZnO films.

(a)

(b)
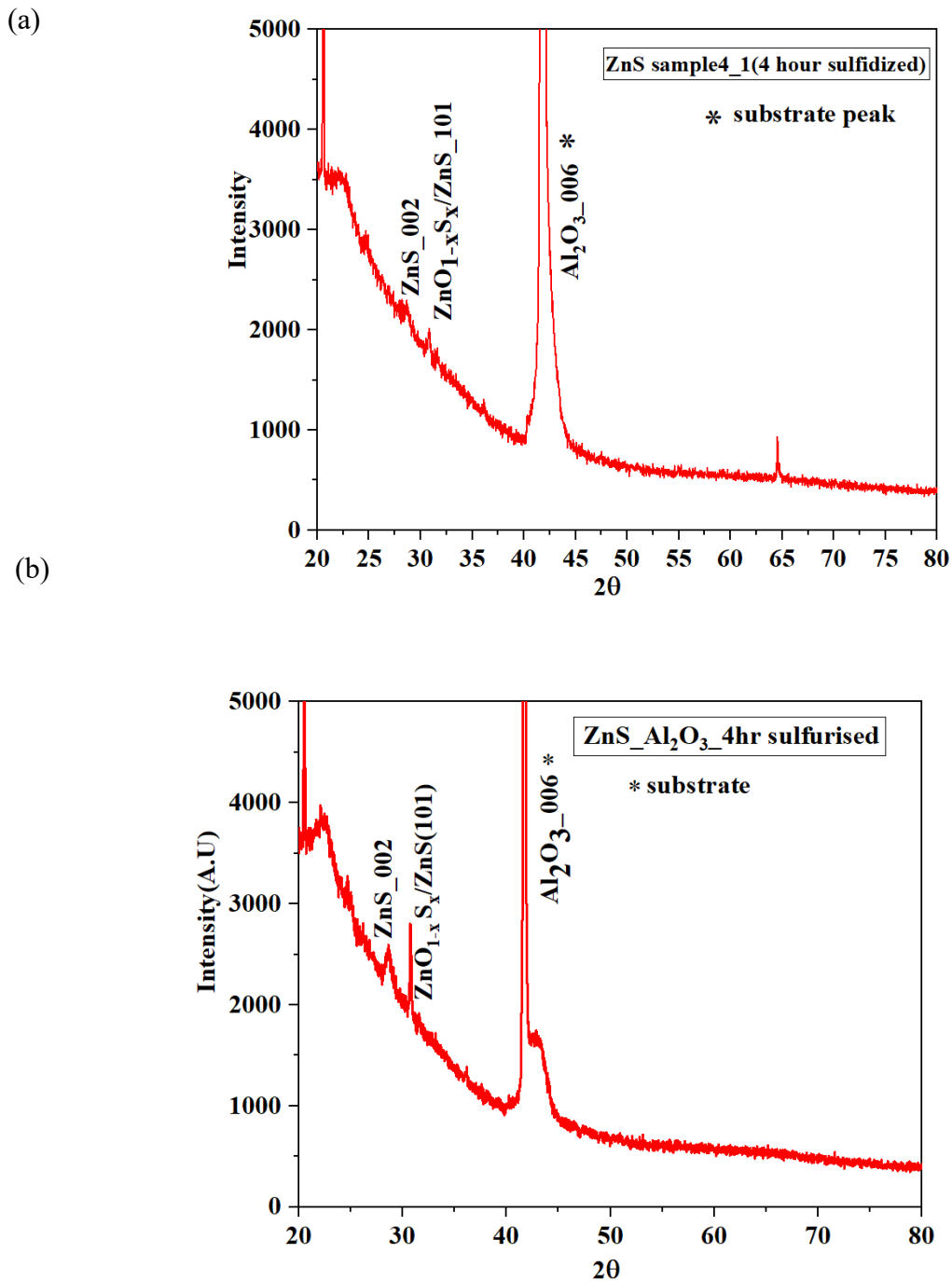
Figure 11: XRD of sulfidized sample (4 hr.) (a) sample1 (b) sample2

From the XRD plot of 1 hour sulfidized film it can be concluded that ZnO has been partially
converted to ZnS which is consistent with the previous result.
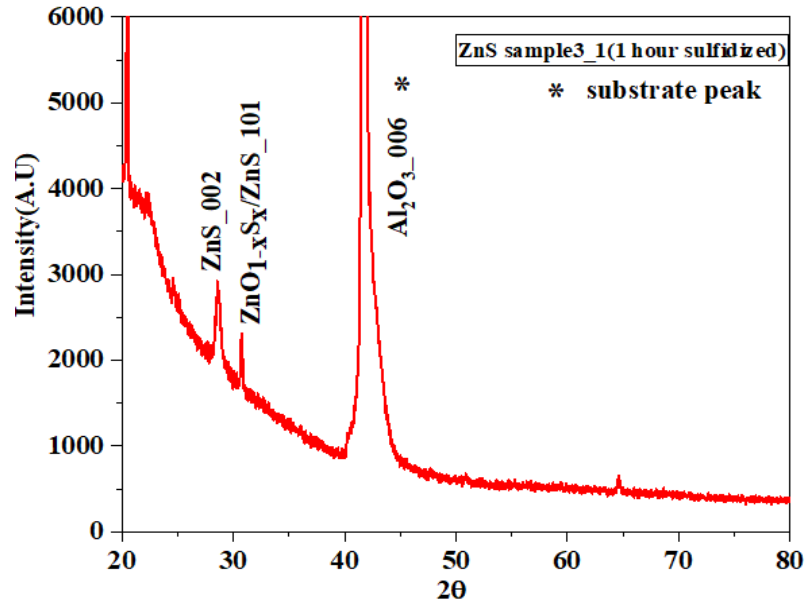
Figure 12: XRD of sulfidized sample (1hr)
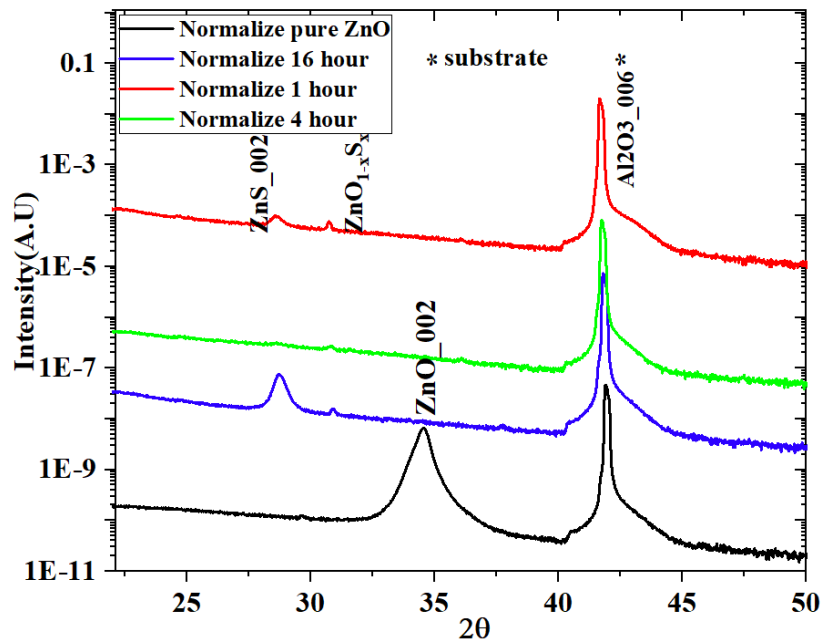
Figure 13: Overlapping plot of parent and sulfidized samples for different time duration

It is evident from all the XRD plot that time and temperature play crucial role in conversion of ZnO to ZnS. The more the exposure time in sulfur environment, the greater the intensity of ZnS (002) peak at any given temperature (180°C).The conversion process involves in-diffusion of sulfur atom in appropriate ZnO crystal lattice site and out diffusion of oxygen.[22] Also comparing the different XRD plots of parent and sulfidized samples it can be observed that wurtzite ZnO (002) has converted to wurtzite ZnS (002) with preferred c-axis orientation. So, it can be concluded that the conversion process of ZnO to ZnS does not alter crystal structure although some paper reported sphalerite phase of ZnS along (111) diffraction peak after conversion.[19] However, for the intermediate peak at $2\theta = 30.8°$, two possible scenarios are there. First, it can be another orientation of wurtzite ZnS phase ZnS (101) or it can be an in between phase $ZnO_{1-x}S_x$. The value of x can be calculated using Vegard's law. Figure 14 shows the lattice parameter vs sulfur mole percent of the mixture which is helpful to determine the lattice parameter at any given composition or if the lattice parameter of a mixed phase is known, the chemical composition of the mixed phase can be predicted. The more the no of sulfur mole percent converted, the higher should be the value of lattice parameter obtained because of larger size of sulfur atom compared to oxygen atom. From the XRD plot of the sulfidized sample I observed that position of the intermediate peak does not shift much depending upon the sulfidation time. So, it is possible that a weak ZnS hexagonal phase developed in between which disappears after the ZnO film undergoes complete sulfidation. The lattice parameters and crystallite size of the sulfidized films are given in the Table 3 and Table 4 respectively. From the Table 3, I see that lattice parameters of wurtzite ZnS matches the theoretical value c= 6.25730Å.[23] The crystallite size of the sulfidized films can be calculated using Debye-Scherrer equation as used earlier for the calculation of crystallite size of parent ZnO films. Apart from

temperature and time, the porosity of the parent film plays major role in sulfidation.

(a)

mixed phase of ZnS_sample1(16hr)

$a_{ZnS}=3.8095Å$

$a_{ZnO}=3.18Å$

$ZnO._{64}S._{46}=3.467Å$

(b)

mixed phase of ZnS_sample3(1hr)

$a_{ZnS}=3.827Å$

$a_{ZnO}=3.192Å$

$ZnO._{626}S._{373}=3.53 Å$
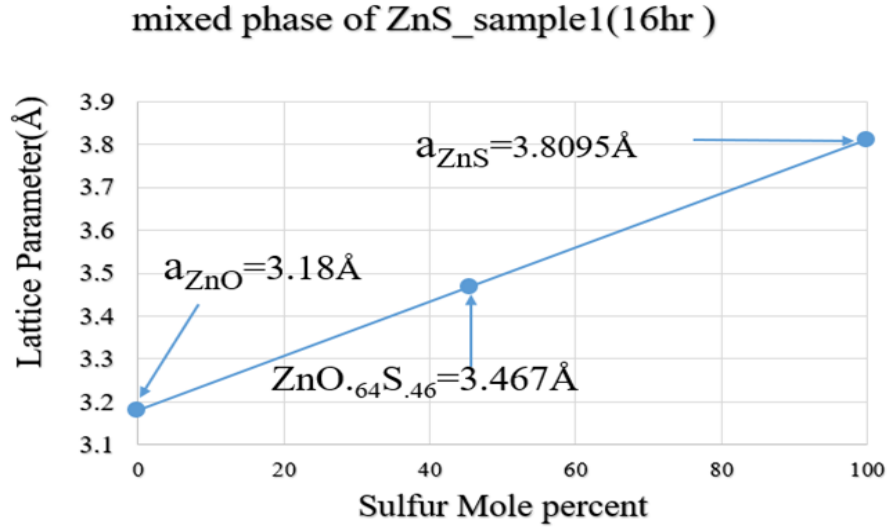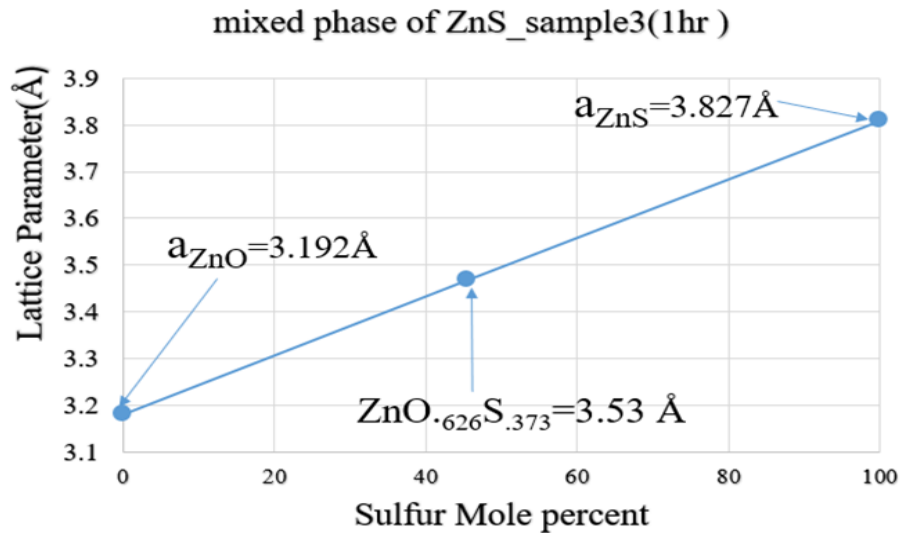
Figure 14: Lattice parameter vs sulfur mole percent (a) 16 hours (b) 1 hour sulfidized films

Research has shown porous ZnO sorbent with gaseous hydrogen sulfide accelerates sulfidation process.[15] The as-prepared ZnO parent films had inherent native defects. These defects affect the migration of dopant atoms during diffusion. From Kirkendall's work it is proved that diffusion mechanism in substitution diffusion must propagate through vacancy formation.

Table 3: Lattice parameters of the sulfidized films

ZnS_sample	2Θ(°)	dhkl(Å)	hkl	a(Å)	c(Å)
1_1	28.74	3.1048	0 0 2	3.81	6.21
3_1	28.59	3.1194	0 0 2	3.827	6.239
4_1	28.72	3.1058	0 0 2	3.81	6.212

Table 4: Crystallite size of the sulfidized samples from porous ZnO

ZnS from porous ZnO	k	FWHM	λ(Å)	Θ(rad)	cosΘ(rad)	ß(rad)	L(nm)	h	k	L
ZnS 16hr	0.9	0.53545	1.5406	0.5013	0.9999	.00935	14.8	0	0	2
ZnS 1hr	0.9	0.51371	1.5406	0.4986	0.9999	.00897	15.4	0	0	2

Studies has shown that for undoped ZnO, sulfidation can be achieved by two processes. First, adsorption of H_2S starts with formation of voids at ZnO/ZnS interface (i.e. the Kerkindall effect).[15] The sulfidation process accompanied by outward growth of ZnS where Zn^{2+} and O^{2-} are transferred to the ZnS/H_2S gas surface. Secondly, sulfidation proceeds by inward growth mechanism where S^{2-} anions diffuse from outward surface to ZnO/ZnS interface internally. ZnO deposition in oxygen atmosphere promotes more porous structure than the vacuum deposition. Also, controlled growth of defects like oxygen vacancies and zinc interstitial affect sulfidation process. By optimizing the background O_2 pressure and post deposition annealing conditions, oxygen vacancies can be controlled in the ZnO films. The sulfidation process discussed so far were employed on more porous films with lot a of inbuilt oxygen vacancies. The

photoluminescence effect of these porous ZnO films which shows strong defect emission peak and weak UV emission peak supports the explanation. Analysis of Field emission scanning microscopy and AFM (atomic force microscopy) revealed that increase of background oxygen pressure converted porous crater -like structure into ZnO nanoparticle. Reduction of the pores resulted from conversion of the pores into nanoparticles as oxygen pressure increased.[24] Figure 15 represents the non-porous parent ZnO and sulfidized samples for 1hour, 16 hours and 32 hours respectively.

From figure 15, it was apparent that the parent ZnO film was highly crystalline in nature with preferred c-axis orientation. The film was deposited in high oxygen pressure (4×10^{-1}mbar) and annealed in 600°c with background O_2 pressure of 100 mbar which was 250 times higher than the annealing pressure used for the previously deposited films. With the increase of annealing temperature and pressure the crystallographic defects such as interstitial atoms, oxygen vacancies, dislocation reduced in a significant rate.[20] But this hinders the probability of sulfidation as migration of the sulfur atoms happens through vacancy propagation. So, I observed that after one hour of sulfidation, no new phase of ZnS appears, and that the ZnO (002) peak was still there with significant reduction of intensity. After 16 hours of sulfidation, we can see that two weak intensity peaks appear at $2\theta = 28.6°$ and $2\theta = 30.8°$ which are ZnS (002) and the intermediate peak $ZnO_{1-x} S_x$/ ZnS (101). After 32 hours of sulfidation a strong peak of ZnS (002) appeared at $2\theta = 28.6°$ and a weak peak appears at $2\theta = 30.8°$ which corresponds to the intermediate phase. If compared the sulfidation process of the previous ZnO films with this new sample, it is noticeable that even after 16 hours of sulfidation not all the ZnO has converted to ZnS. Additionally, 32 hours of sulfidation was also not long enough time for complete conversion of ZnO to ZnS. Apart from that, two more weak intensity peaks appear at $2\theta = 47.8°$

and $2\theta = 56.7°$ which corresponds to wurtzite ZnS (2 -1 0) and ZnS (2 -1 2) phases which means the sulfidized film became polycrystalline in nature compared to preferential c-axis oriented film.
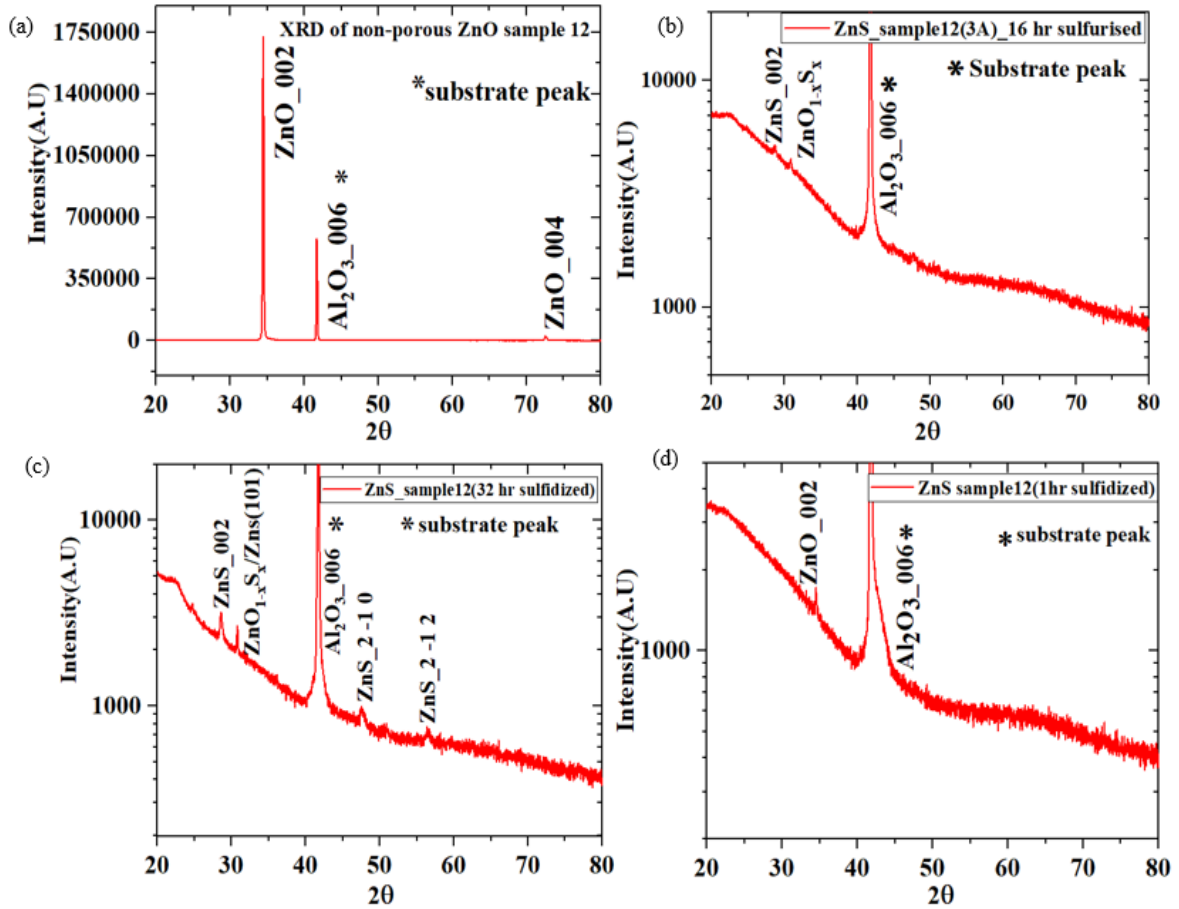
Figure 15: XRD of a) nonporous parent ZnO, b) 16 hours sulfidized ZnO, c) 32 hours sulfidized ZnO, and d) 1 hour sulfidized ZnO

The most plausible reason of slow rate of sulfidation must be vacancy formation which was not prevalent in non-porous parent ZnO film annealed in high oxygen background. Indeed, the photoluminescence spectra of this parent film has strong UV emission peak compared to the

previous ZnO films which implies that oxygen vacancies were reduced significantly that were not helpful in migration of S^{2-} ions through the lattice. The Figure 16 represents the comparison of 16-hour sulfidation in 180°C for porous and non-porous films. Figure 17 represents the overlapping Plot of sulfidation of non-porous ZnO films for different time duration.
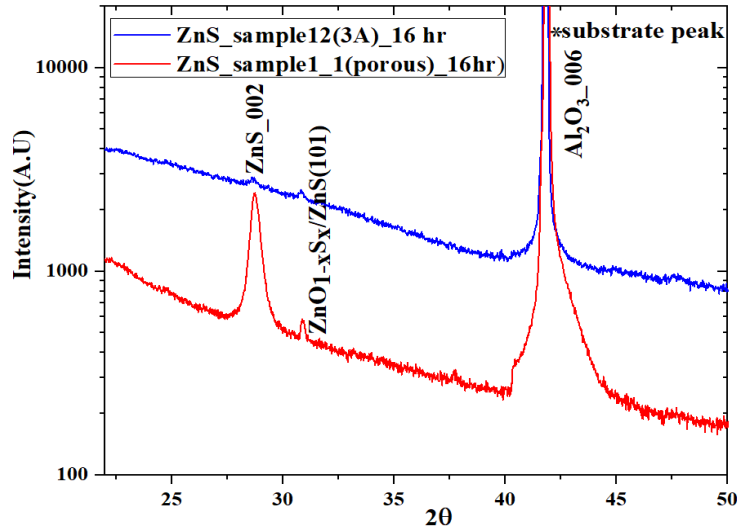
Figure 16: comparison of sulfidation for porous and non-porous film for 16 hours
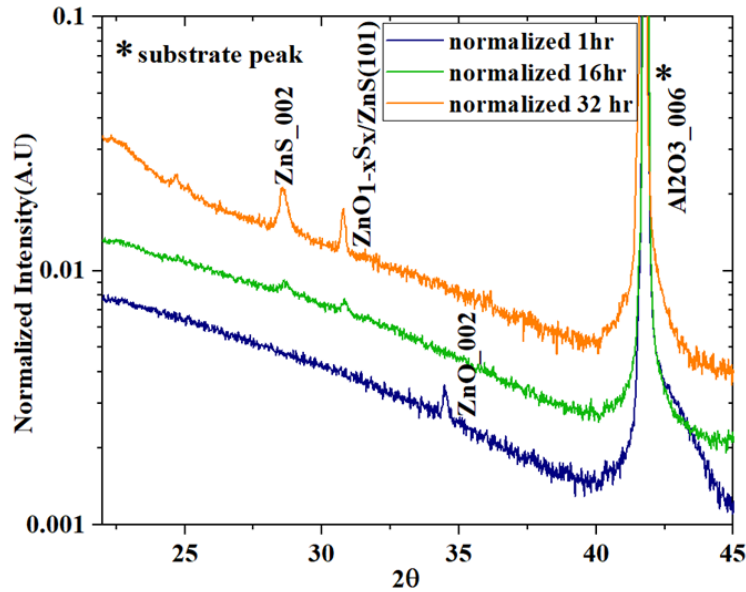
Figure 17: Overlapping XRD plots of sulfidized non-porous ZnO films for different time duration

27

The lattice parameters of these non-porous parent sample and sulfidized samples can be represented in Table 5 and Table 6 respectively. Table 7 shows crystallite size of the sulfidized films from non-porous ZnO. I observed that the FWHM of the ZnS sample from non-porous films are higher than the parent ZnO film. Crystallinity of sulfidized samples had degraded compared to parent ZnO samples.

Table 5: Lattice parameter of non-porous parent ZnO sample

ZnO non-porous Parent Sample	$2\Theta(°)$	$d_{hkl}(Å)$	hkl	a(Å)	c(Å)
12	34.45	2.601	0 0 2	3.192	5.203

Table 6: Lattice parameter of ZnS sample 12 sulfidized for different amount of time.

ZnS_sample 12	$2\Theta(°)$	$d_{hkl}(Å)$	hkl	a(Å)	c(Å)
12_3A	28.64	3.1144	0 0 2	3.821	6.229
12_3B	28.58	3.12	0 0 2	3.83	6.242
12_2B	34.48	2.6	0 0 2	3.19	5.198

Table 7: Crystallite size of non-porous sulfidized ZnO sample

Non-Porous parent sample ZnS sample	k	FWHM	$\lambda(Å)$	Θ(radian)	$\cos\Theta$(radian)	ß(radian)	L(nm)	h	k	L
12_3A	0.9	0.4706	1.5406	0.2499	0.9999	0.008213519	16.8	0	0	2
12_3B	0.9	0.35945	1.5406	0.2494	0.999	0.006273586	22.1	0	0	2
12_2B	0.9	0.17756	1.5406	0.3008	0.9999	0.003099007	44.7	0	0	2

The average experimental lattice parameter c= 6.236Å is matched with the reported value

c=6.25Å.[23]

SEM and EDS were performed on both the parent and sulfidized samples. Gold coating

was deposited on the parent sample and carbon coating was deposited on the sulfidized sample

for 30 seconds. Figure 18 shows SEM picture of the ZnO sample which was sulfidized for 16

hours. From the SEM picture it was apparent that the surface of parent ZnO sample was smooth

but after sulfidation of 16 hours the surface became rough and showed distribution like lamellar

structure. The figure 19 represents the EDS spectra of the sulfidized film.
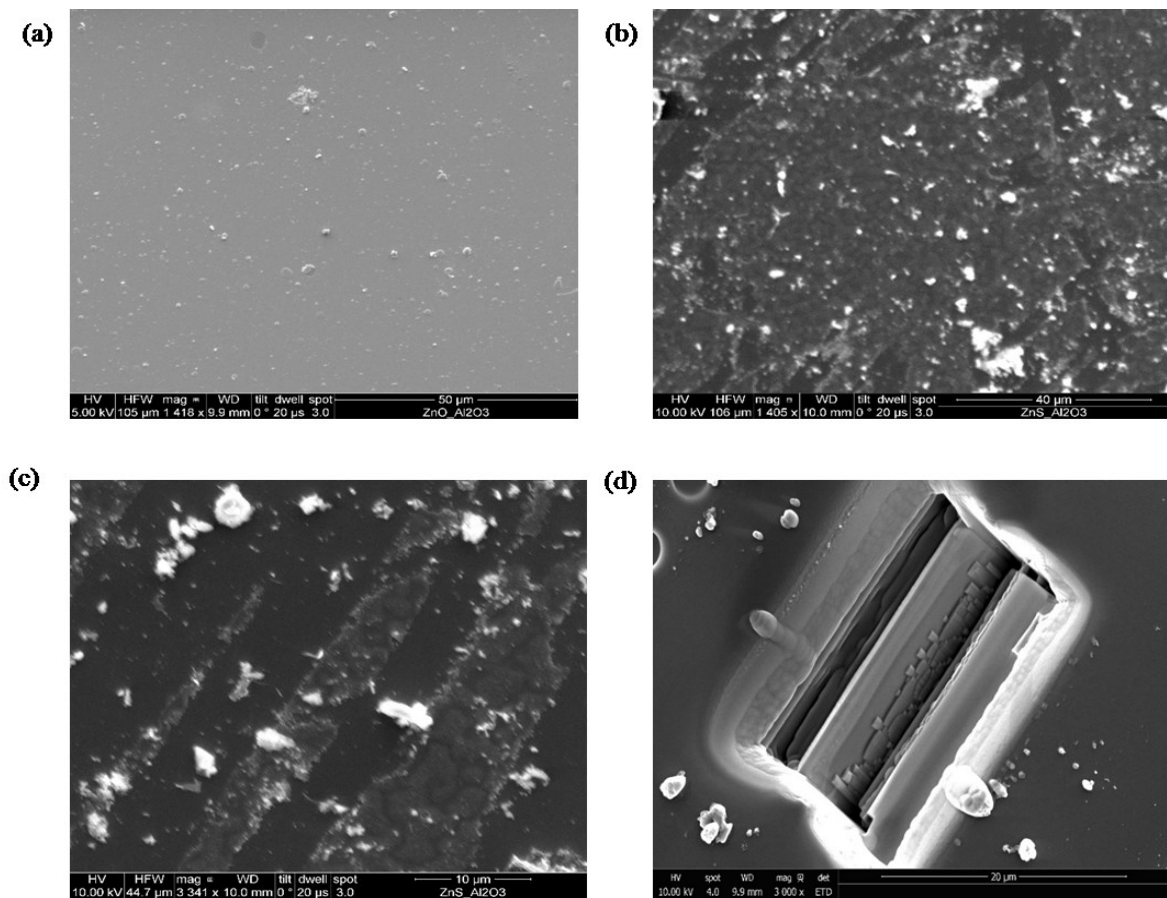
Figure 18: SEM micrographs of (a) parent sample and 16hr sulfidized sample (b)40μm (c) 10μm (d) 20μm

From the figure below, the constitutional elements of the sulfidized film can be seen.
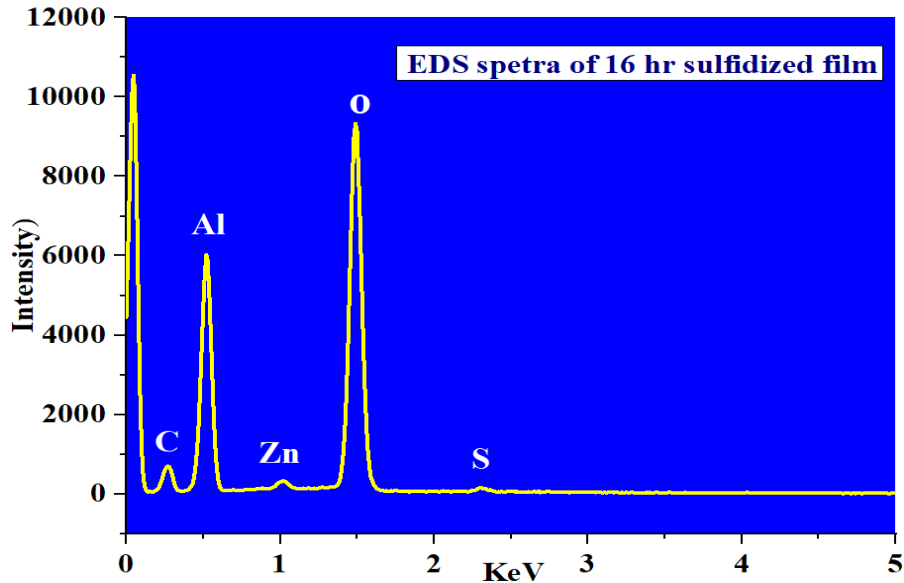
Figure 19: EDS spectra of the sulfidized sample

Raman spectroscopy was employed to study the vibrational energy modes in the system. Raman spectroscopy can give information about the defects presents in the crystal structure, bond force constant or the interaction between the atoms. The basic principle of Raman spectroscopy is based on inelastic scattering of monochromatic light (laser source) after the interaction with a sample that is Raman active. In inelastic scattering, the frequency of the scattered light gets shifted up or down compared to the excitation frequency, which is called Raman effect. A photon is absorbed by the material and jumps into higher vibrational energy state. When it falls back to a lower energy level, three phenomena can happen. It can fall back to same energy state as excitation energy which is called Rayleigh scattering. Or it can have a transition to a lower or higher energy state, which are called Anti-Stoke or Stokes scattering respectively. Stokes scattering was studied for both porous and non-porous parent ZnO and the

sulfidized samples.

Wurtzite ZnO with C_{6v} point group symmetry has six Raman active modes. Those are two A_1, two E_1, two E_2 modes. Figure 20 shows Raman active modes for ZnO nanoparticles. The frequencies of the fundamental modes of standard ZnO nanoparticles are A1(TO) = 382 cm^{-1}, A1(LO) = 574 cm^{-1}, E2 (high) = 438 cm^{-1}, E1(LO) = 583 cm^{-1}. The second order mode appears at 334 cm^{-1}. Other modes that are reported in literature[25] E2(low) = 101cm^{-1}, E1(TO) = 407 cm^{-1} which didn't appear in the standard sample. The low frequency E2 mode corresponds to the vibration of Zn atoms and the high frequency E2 mode is associated with oxygen atoms.[25] For strong preferentially oriented ZnO films when incident light is normal to the surface, only A1(LO) and E2 modes are detected and other modes become forbidden.[25]
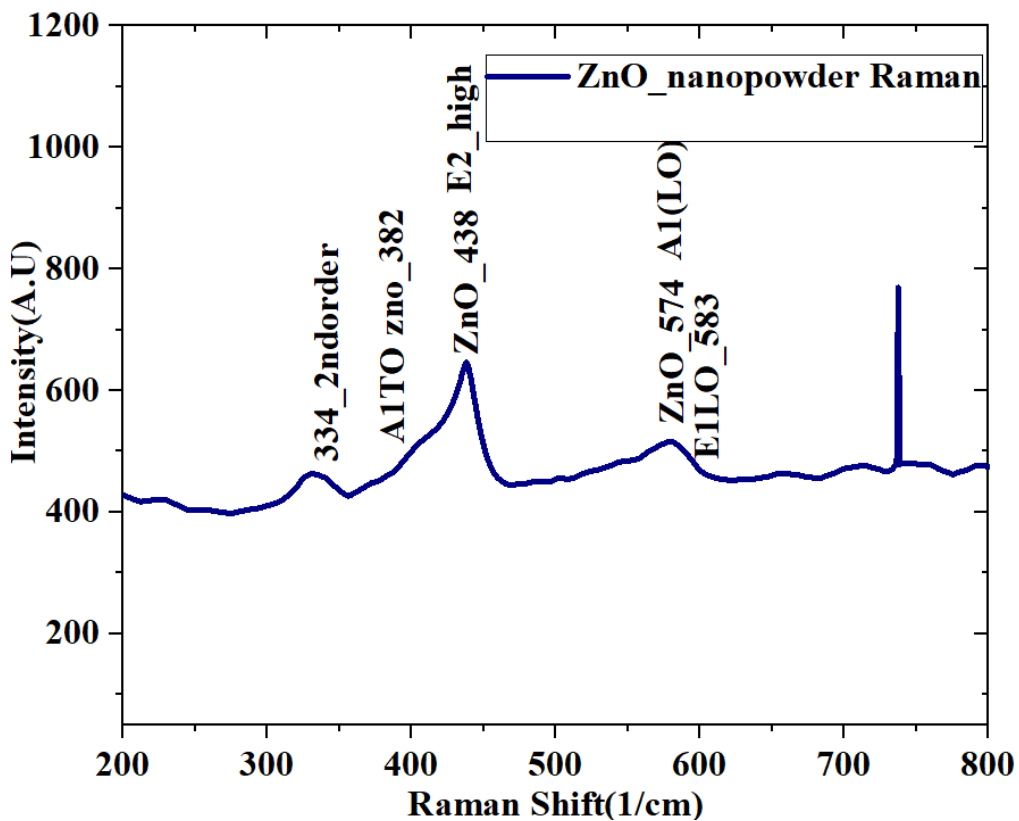
Figure 20: Raman active modes of ZnO nanoparticles

However, for the porous ZnO sample observed modes are 334, 378, 416, 574 cm^{-1}. 334 cm^{-1} is the second order vibrational mode as mentioned earlier. The peak at 378 cm^{-1} can be attributed to A1(TO) symmetry mode which matched with the reported value in the paper by Wei *et al.*[26] The mode at 416 cm^{-1} corresponds to the sapphire substrate. The peak around 574 cm^{-1} can be deconvoluted according to Lorentzian distribution. Figure 21 shows the overlapping plot of Raman active modes of porous ZnO film, ZnO Nano powder and sapphire substrate. Figure 22 shows the peak fitting around 574 cm^{-1}. The peak around ~ 575 cm^{-1} can be also attributed to Raman active mode of sapphire substrate. Another peak observed around 581 cm^{-1} corresponds to E1(LO) mode which according to Wei *et al.*[26] comes from prevalence of oxygen vacancies in the deposited film.
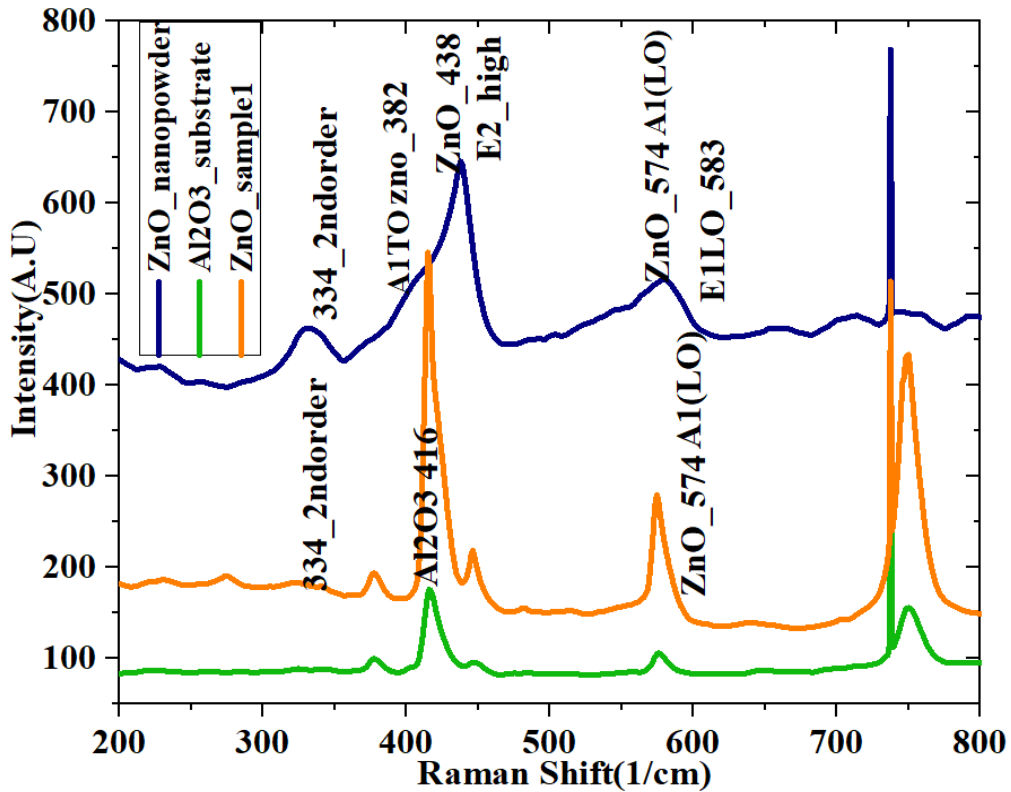
Figure 21: Overlapping plots of porous ZnO film with the ZnO Nano powder

The oxygen vacancy related defects can be resolved by annealing the films in oxygen rich atmosphere. Wei *et al.*[26] also reported another peak around 560 cm^{-1} which didn't appear in the porous ZnO film. They attributed this peak is observed due to incomplete oxidation of Zn in their experiment. According to that paper ZnO contains large number of voids that can trap interstitial zinc atoms which didn't get oxidized. Figure 23 shows the Raman active modes of non-porous ZnO thin film. Raman spectroscopy of the porous sulfidized films were studied as well.
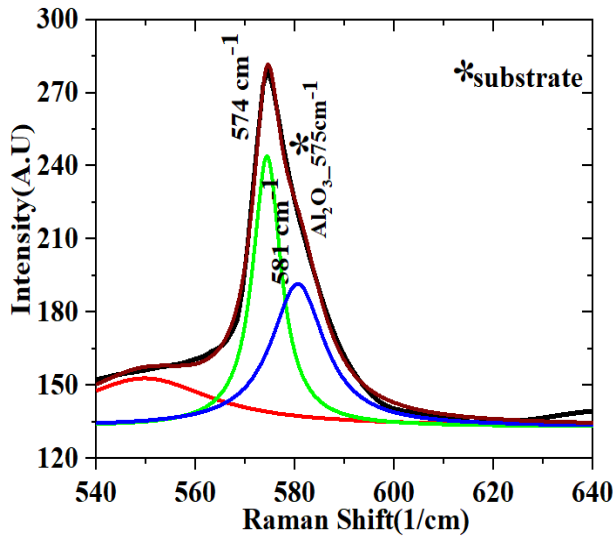
Figure 22: Deconvolution of peak of 574 cm^{-1}
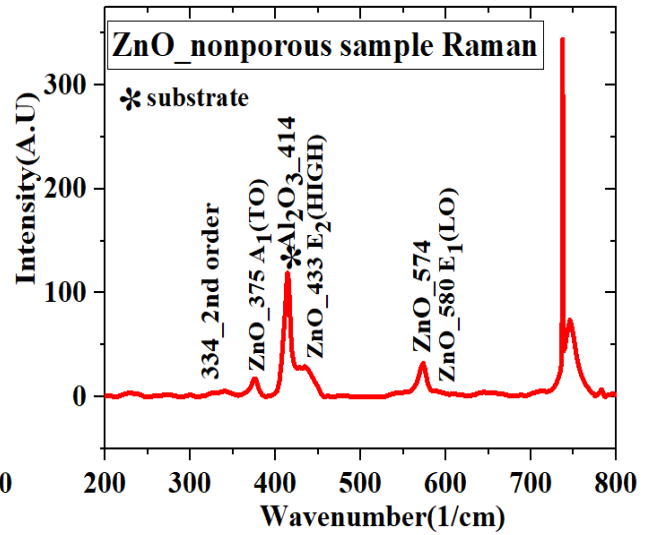
Figure 23: Raman active modes of non-porous ZnO

Wurtzite ZnS belong to space group C6$_3$mc having two formula units per primitive cell. The Raman active modes for ZnS are one A1, one E1, two E2 and two B2 where A1 and E1 modes are both Raman and IR active. 2E2 pair are only Raman active. Figure 24 shows the Raman spectroscopy plot of a sulfidized film. The Raman spectrum of wurtzite ZnS was collected at room temperature. A first order scattering at 347 cm^{-1} which corresponds to A1 and E1 symmetry LO

modes was observed.
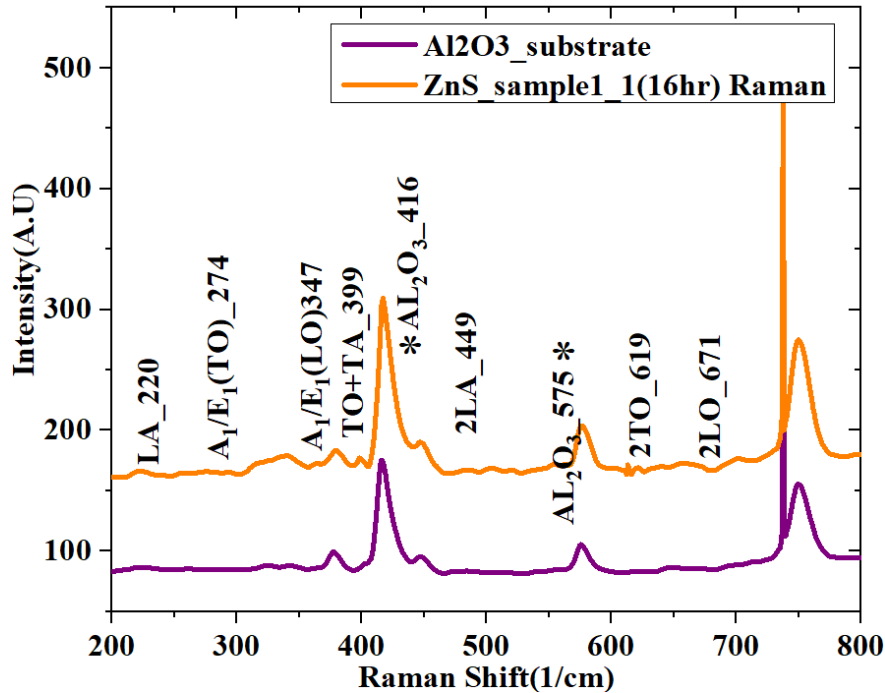
Figure 24: Raman active mode of sulfidized sample for 16 hours

At ~274 cm^{-1} we observe two low frequency doublets assigned as A1/E1(TO) mode. Xiong *et al.*[27] reported A1/E1(TO) mode at 269 cm^{-1} for their ZnS nanowires which is shifted for the thin film. They also reported another mode at 335 cm^{-1} which was not visible in the bulk sample. That peak is due to surface phonon scattering. According to that paper in the ZnS nanowire, surface optical phonon mode (SO) should not be observed because of perfect crystal symmetry and smooth surface. This Raman active mode was observed in the sulfidized film. The Figure 25 shows the surface optical phonon mode (SO) and E1(LO) modes. Figure 26 represents Raman spectra of 1 hour sulfidized film. According to Brafman and Mitra E2 modes are reported around 72 and 286 cm^{-1} [28] which did not appear in the sulfidized film for this experiment.

Deconvolution of the spectra around 340 cm^{-1} shows the surface active phonon mode ~ 335 cm^{-1}.
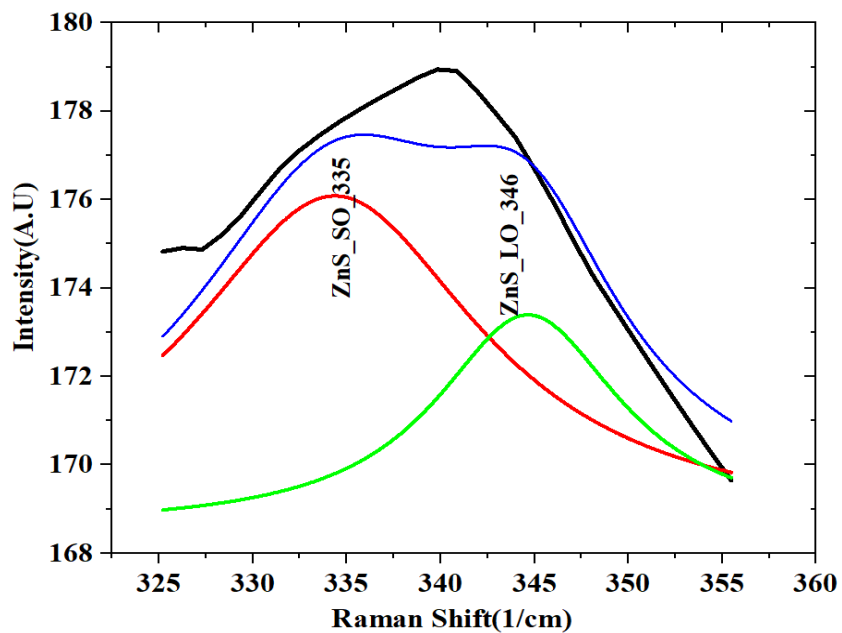
Figure 25: Deconvolution of Raman active modes (LO/SO)
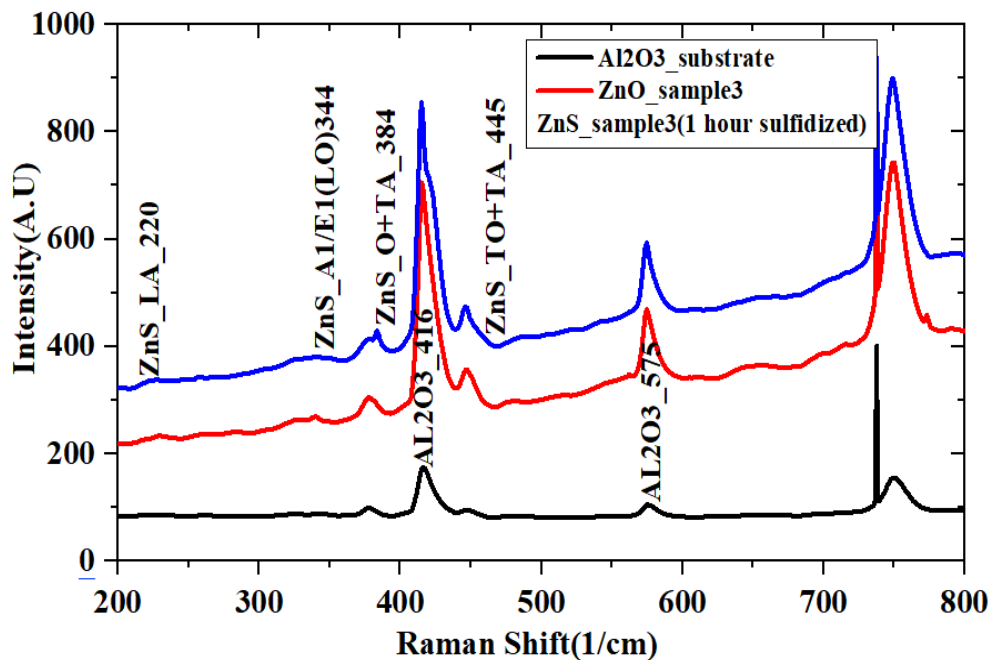
Figure 26: Raman spectra of ZnS sample (sulfidized for 1 hour)

The TO modes with A1 and E1 symmetry were reported at 273 cm^{-1} which matched with our experiment. The LO modes of A1 and E1 symmetry were assigned at 351cm^{-1} which appears for our experiment at 347 cm^{-1}. Other group of researchers found TO mode around 274 cm^{-1} and LO mode around 352 cm^{-1} at room temperature.[29] Schneider and Kirby reported E1(LO) to be around 348 cm^{-1}. [30] Ebisuzaki and Nicol found A1/E1(LO) mode around 350 cm^{-1}. [31] The ZnS thin film Raman spectroscopy in our experiment is matched with reported values of other papers. For the 2nd order Raman scattering the total region can be subdivided into three regions. i) low frequency region (0-400 cm^{-1}) where acoustic overtones are visible, ii) Intermediate frequency region (400-540 cm^{-1}) dominated by both optical and acoustic phonon, iii) high-frequency region (540-750) dominated by optical overtone and combinations. In the low frequency region, we can see a weak peak corresponds to acoustic overtone mode as LA (220 cm^{-1}). The broad weak peak around ~ 400 cm^{-1} can be assigned as TO+TA mode. The peak around ~619 and 671 can be assigned as 2TO and 2LO modes. Cheng *et al.*[32] reported LA overtone mode at 219 cm^{-1}. And the peaks around 622 and 676 cm^{-1} were assigned as 2TO and 2LO modes. Table 8 provides the comparison between the experimental and reported value of the Raman active modes of porous ZnO thin film. Table 9 represents the comparison of the reported and experimental values of the Raman active modes of ZnS samples sulfidized from porous parent ZnO.

Table 8: Experimental and reported value of Raman active modes for porous ZnO thin film

Active Modes	My Work	Reported Modes(cm^{-1})
A1(TO)	378	380
A1(LO)	574	574
E1(TO)	not observed	407
E1(LO)	581	583
E2(HIGH)	not observed	437
E2(LOW)	not observed	101
2nd order mode	334	334

Table 9: Comparison of the Raman active modes of reported and experimental data of ZnS

ZnS Raman active modes	wavenumber(1/cm)		
	literature reference	bulk	my work
LA	216	217,219	220
A1/E1(TO)	269	267,273,274,276,283	274
E2(TO)	282		not observed
A1/E1L(O)	346.4	348,350,351,352	347
SO	335	not observed	335
2TO	615	617	619
TO+LA	400,633	642	399
2LO	668	673	671

In photoluminescence spectra of ZnO, there are two regions: Ultraviolet (UV) emission band and visible emission band (green, yellow, blue, violet and orange). The UV emission is characteristic emission of ZnO which happens due to exciton combination or near band edge transition.[33] The emission in the visible region is attributed to the intrinsic or the extrinsic defect in ZnO.[33] The Figures 27 and 28 shows the photoluminescence spectra of porous and non-porous ZnO thin film. From the PL spectra of porous ZnO film, we can observe two emission peaks around 380 nm and 510nm. The weak UV emission peak around 380 nm is attributed to exciton recombination from conduction to valence band. The peak around 516 nm is related to defect emission peak which is green emission. ZnO has several intrinsic defects that causes defect emission peaks. i) oxygen vacancy (V_o),ii) zinc vacancy (V_{zn}), iii) interstitial oxygen (O_i), iv) interstitial zinc (Zn_i), v) oxygen atom at position of zinc (O_{zn}), vi) zinc atom in position of oxygen(Zn_o).[34] The formation energy of zinc vacancy (V_{zn}) is much larger than oxygen vacancy (V_o) (5.4ev> 3ev). So, the probability of formation of oxygen vacancy is much higher than the probability of zinc vacancy.

It is hypothesized that transition between singly ionized oxygen vacancies and photoexcited holes is responsible for green emission.[33]
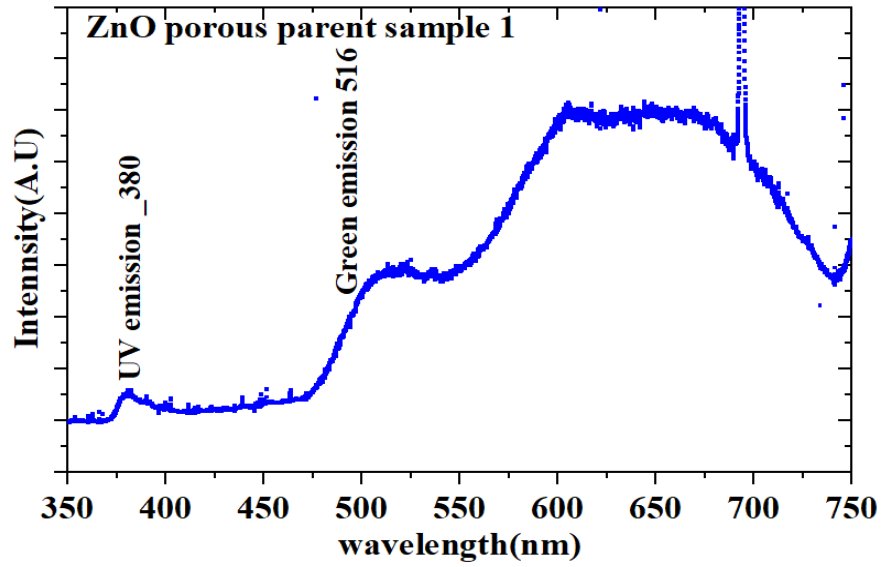

Figure 27: PL spectra of porous ZnO thin film
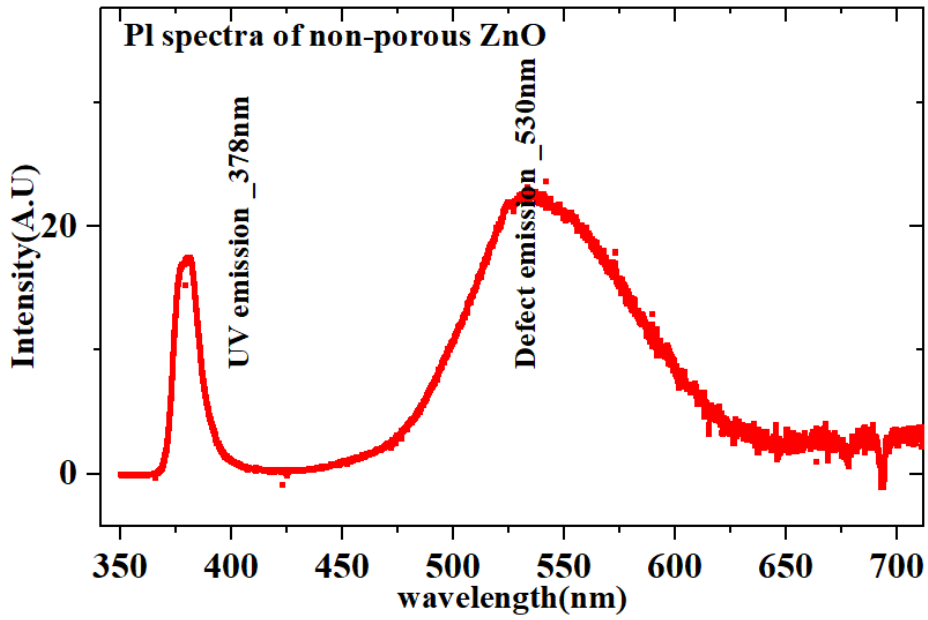
Figure 28: PL spectra of non-porous ZnO thin film

The yellow orange emission was attributed to the prevalence of interstitial oxygen and dislocation present in the film.[33] ZnO has intrinsic defects like oxygen vacancies, Zn interstitials which decreases the probability of near band edge excitonic recombination compared to the non-radiative recombination attributed to the different defects present in the crystal. If I compare this PL spectra of the porous and the non-porous film, I can see that the UV emission peak ~380 nm has improved significantly, and the defect related peak is not as intense as compared to the porous film. This phenomenon can be attributed to the reduction of oxygen vacancies for the non-porous film as it was grown and annealed in more oxygen rich atmosphere (100 mbar O_2 pressure) than the porous film (annealed in 3×10^3 mbar O_2 pressure). Zhaoyang *et al.*[34] proposed that defect green emission with higher intensity happens because of high oxygen pressure in the sample. O_{zn} is more responsible for green emission compared to V_o. However, Jin *et al.*[35] suggested that stoichiometry of ZnO thin films can be improved if the films can be grown in high oxygen pressure. He suggested that ZnO thin films generally have lot of oxygen vacancies resulting in poor stoichiometry. Annealing the films in high oxygen pressure has more improved stoichiometry resulting in low oxygen vacancies and interstitial atoms. The XRD result of highly crystalline quality and improved UV emission spectra of the non-porous ZnO film supports these explanations. Wei *et al.*[26] in the paper discussed that Zn vacancy acceptor level is around 2.6ev. They observed blue emission from the PL spectra of their film which is of value 2.66 ev almost close to 2.6ev. The source of blue emission is electronic transition from interstitial donor level (Zn_i) to the acceptor level attributed to zinc vacancy (V_{zn}). Other group of researchers found that concentration of oxygen vacancies (V_o) and zinc interstitial (Zn_i) is proportional to annealing oxygen pressure as $(PO_2)^{-1/2}$ but the zinc vacancy concentration is proportional to $(PO_2)^{1/2}$. Given this fact, concentration of zinc vacancies can also increase the probability of the non-radiative

transition. Figures 29 and 30 represents the PL spectra of ZnO porous sample 3 and bulk ZnO sample respectively. From the deconvoluted PL spectra of the porous ZnO sample, it can be observed that the low intensity UV emission peak around 426 nm was red shifted in comparison with the standard bulk sample.
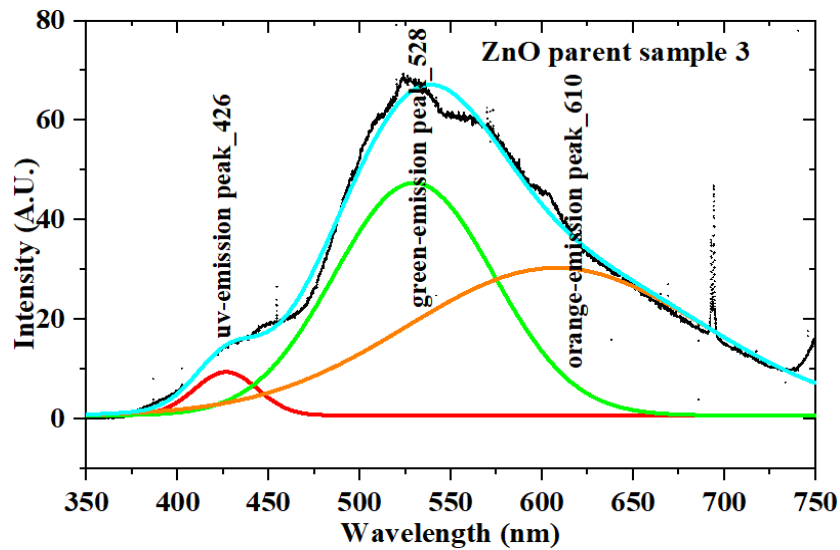
Figure 29: PL spectra of porous ZnO sample 3
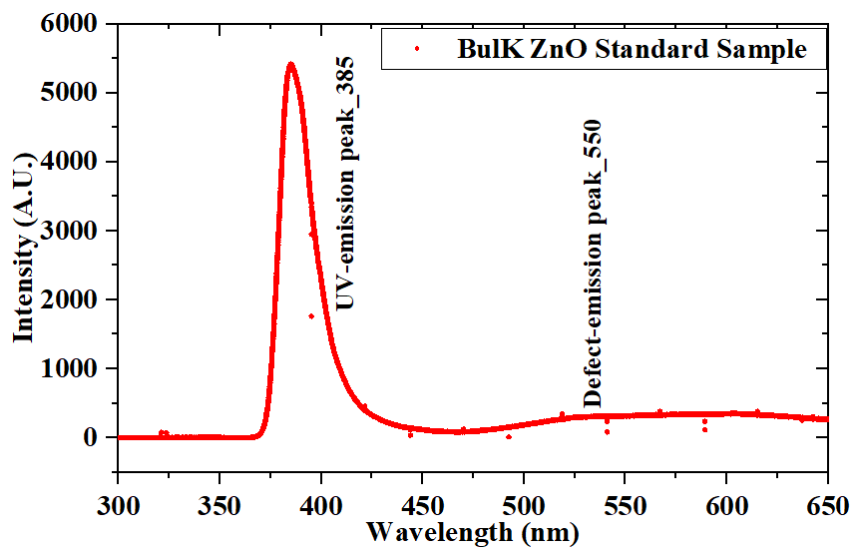
Figure 30: PL spectra of bulk ZnO sample

In deconvoluted PL spectra of the porous ZnO sample, the low intensity UV emission peak around 426 nm which was red shifted with respect to the standard bulk sample, might be possibly the blue emission[26] which typically happens due to prevalence of oxygen vacancies in the thin film sample. However, with the comparison of non-porous ZnO sample to the bulk sample we find the UV emission spectra intensity is quite high as well as the defect spectra. The most plausible explanation would be annealing in high oxygen pressure might have reduced the oxygen vacancies and increased the zinc vacancies.[35] So far, defects related emission of ZnO has remained controversial for decades and the details of electronic transition are still not very clear yet till date. PL of the sulfidized films also dependent on the sulfidation environment, time, and the defects present in the crystals. The Figure 31 represents the PL spectra of the sample which was sulfidized for 16 hours (Excitation wavelength 325 nm).
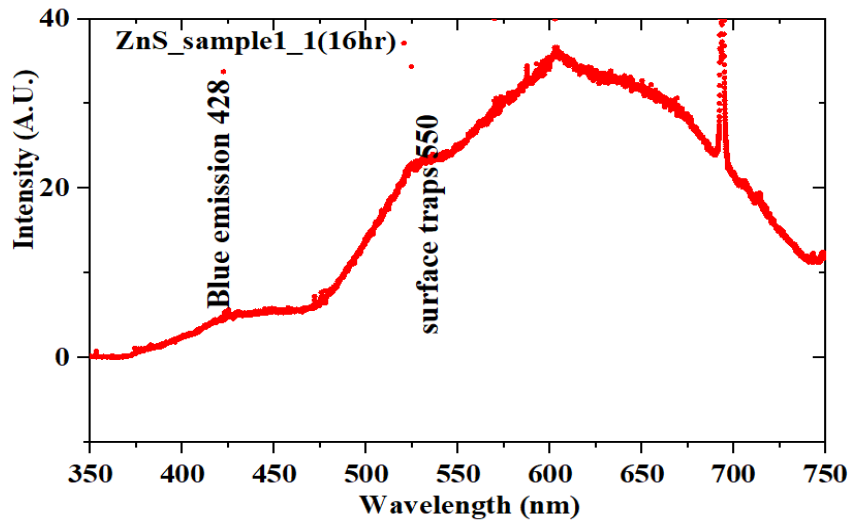
Figure 31: PL spectra of the film sulfidized for 16 hours

From the PL spectra of the sulfidized film I observed that the spectral shape was broad and asymmetric. Researchers have reported blue emission band at 428 nm from ZnS. Becker and

Bard suggested the blue emission due to sulfur vacancies (S^{-2}).[36] Other group of researchers suggested blue emission around 470 nm due to Zn^{+2} acceptor ions. Denzler *et al.* [37]reported four types of point defects which create intermediate trap levels inside the band gap. Zinc and sulfur vacancies and interstitial atoms create four optical transition steps causing emission at longer wavelength. The experimental value of optical band gap (2.8ev) of the sulfidized film was lower than the theoretical optical band gap (3.8ev). Due to the increased surface to volume ratio because of the lower crystallite size the probability of excitonic transition decreases compared to the non-radiative surface transition due to induced trap levels. Figure 32 represents the plot of another porous sample which was sulfidized for 1 hour. From this plot, the appearance of blue emission band around 428nm .
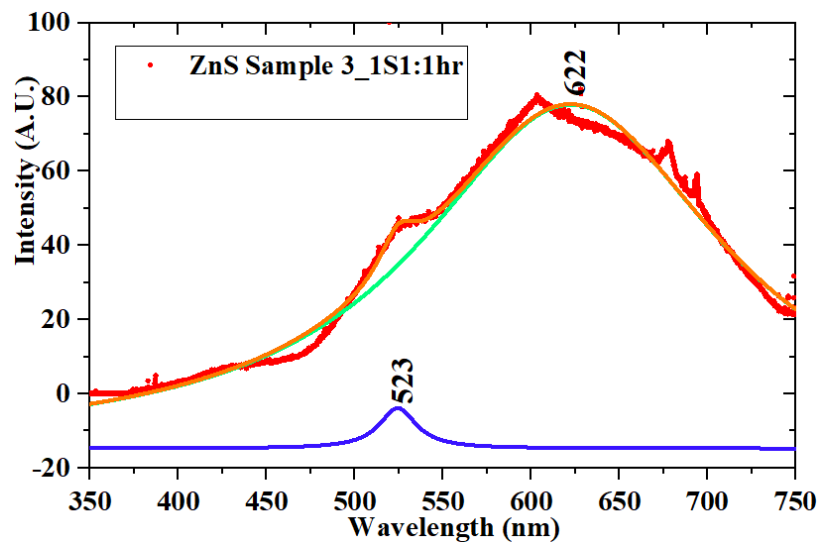
Figure 32: PL spectra of the porous sulfidized film (1 hour)

A weak shoulder peak around 523 nm was seen which can be attributed to the recombination of the electron hole pair on the surface traps that lies between the band gap. Hu *et al.*[38] observed

emission in green region and attributed the self-activated centers containing vacancies and the interstitial states as the surface traps. Figure 33 ,34 and 35 represents the PL spectra of the non-porous films which were sulfidized for 16 hours,32 hours and 1 hour respectively.
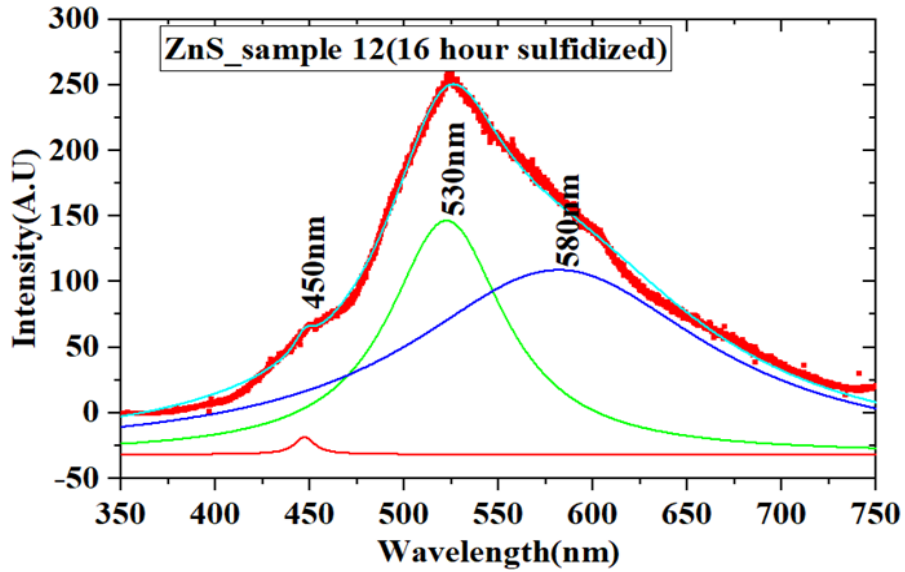
Figure 33: PL spectra of ZnS sample12(16 hour sulfidized)
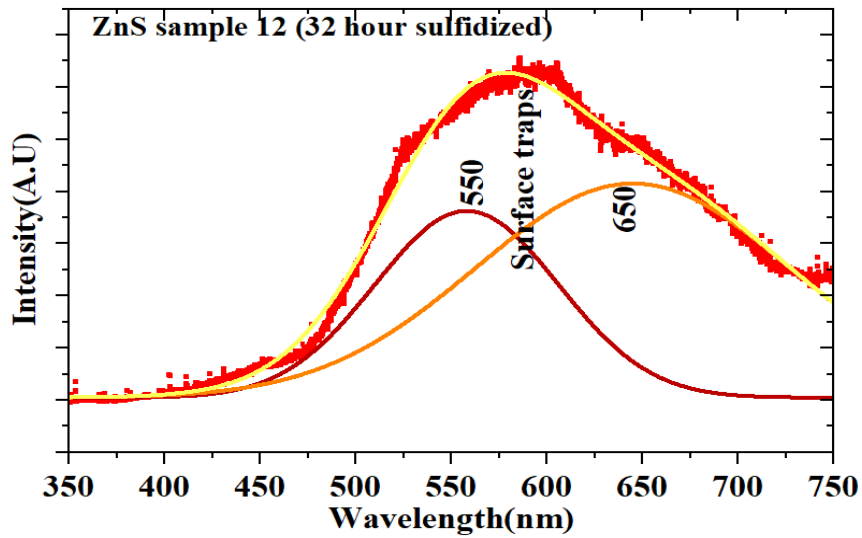
Figure 34: PL spectra of ZnS sample12(32 hour sulfidized)

From the Figure of non-porous film, which was sulfidized for 16 hours, blue emission band attributed to sulfur vacancy (S^{-2}) appeared at 450 nm instead of 428 nm as resulted for the porous sulfidized films. The reason for the red shift in this emission band has not yet been reported. Though Bhattacharjee and Lu reported red shift of the blue emission band due to increase of annealing temperature.[39] The reason for red shift in our samples needs more investigation. For the film which was sulfidized 32 hours no blue emission band around 428nm was observed. Most plausible explanation would be less sulfur vacancy due to more exposure time in sulfur rich environment. Two other bands around 550 nm and 650 nm appear for surface traps present in the band gap.
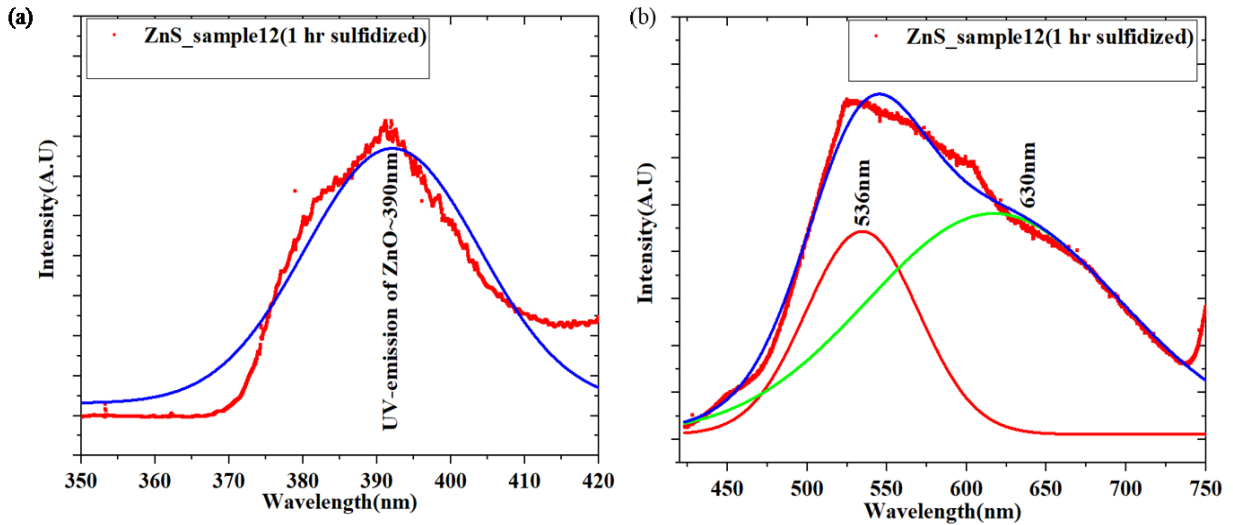
Figure 35: PL spectra of sample12 (1 hour sulfidized) (a) UV emission and (b) defect emission

From the deconvoluted spectra of the film which was sulfidized for 1 hour, presence of characteristic UV emission peak of ZnO around 390 nm was evident and the defect emission peaks around ~ 540 nm and 640 nm which could be caused by prevalence of surface defect states

inside the band gap were also observed.

From the XRD, Raman spectra, and PL spectra analysis it is observed that ZnO thin films are converted to ZnS thin films which is highly dependent upon sulfidation time and temperature. Sulfidation time and temperature play an important role controlling the stoichiometry of the films. At any certain temperature the sulfidation is dependent on the exposure time on the sulfur environment. The more the exposure time, the more layers of ZnO will get sulfidized. However, vacancy plays an important role for migration of the sulfur atoms through the crystal lattice. Whether the parent ZnO film is porous or not, PL and Raman spectroscopy can provide lot of details about the stoichiometry of the parent ZnO films. For instance, the strong UV emission intensity defines less oxygen vacancy and better stoichiometry of the ZnO films. Though sulfidation may not be very fast because lesser vacancies make it difficult for the sulfur atoms to move through the lattice and replace the oxygen. For non-porous parent films, it needs more exposure time in the sulfur environment to sulfidize the films when porous defective ZnO films might have poor stoichiometry but those got better sulfidized for various reasons discussed through each section. Additionally, as diffusion of S^{2-} anions are essentially temperature dependent it would be worthwhile to study the onset of diffusion process by varying the temperature of sulfidation while keeping the time of sulfidation constant. As part of my experiment, I have explored the temperature dependence on the sulfidation process which caused structural variation of the sulfidized films through XRD analysis. Figure 36 represents the XRD of porous ZnO parent sample and the comparison of XRD of the sulfidized films which were sulfidized for 4 hours at 100°C and 180°C.

From the figure I saw that the sulfidized film at 100°C has an evident peak of wurtzite ZnO at around $2\theta \sim 34.5°$ whereas the film which was sulfidized at 180°C had no presence of

ZnO. A new phase of wurtzite ZnS (002) developed around $2\theta \sim 28.6°$ followed by complete sulfidation of porous ZnO at 180°C. No intermediate peak around $2\theta \sim 30.7°$ which corresponds to $ZnO_{1-x} S_x$ / ZnS (101) was observed. A weak peak of $ZnO_{1-x}S_x$/ ZnS (101) grew around $2\theta \sim 30.7°$was also seen.

(a)

(b)
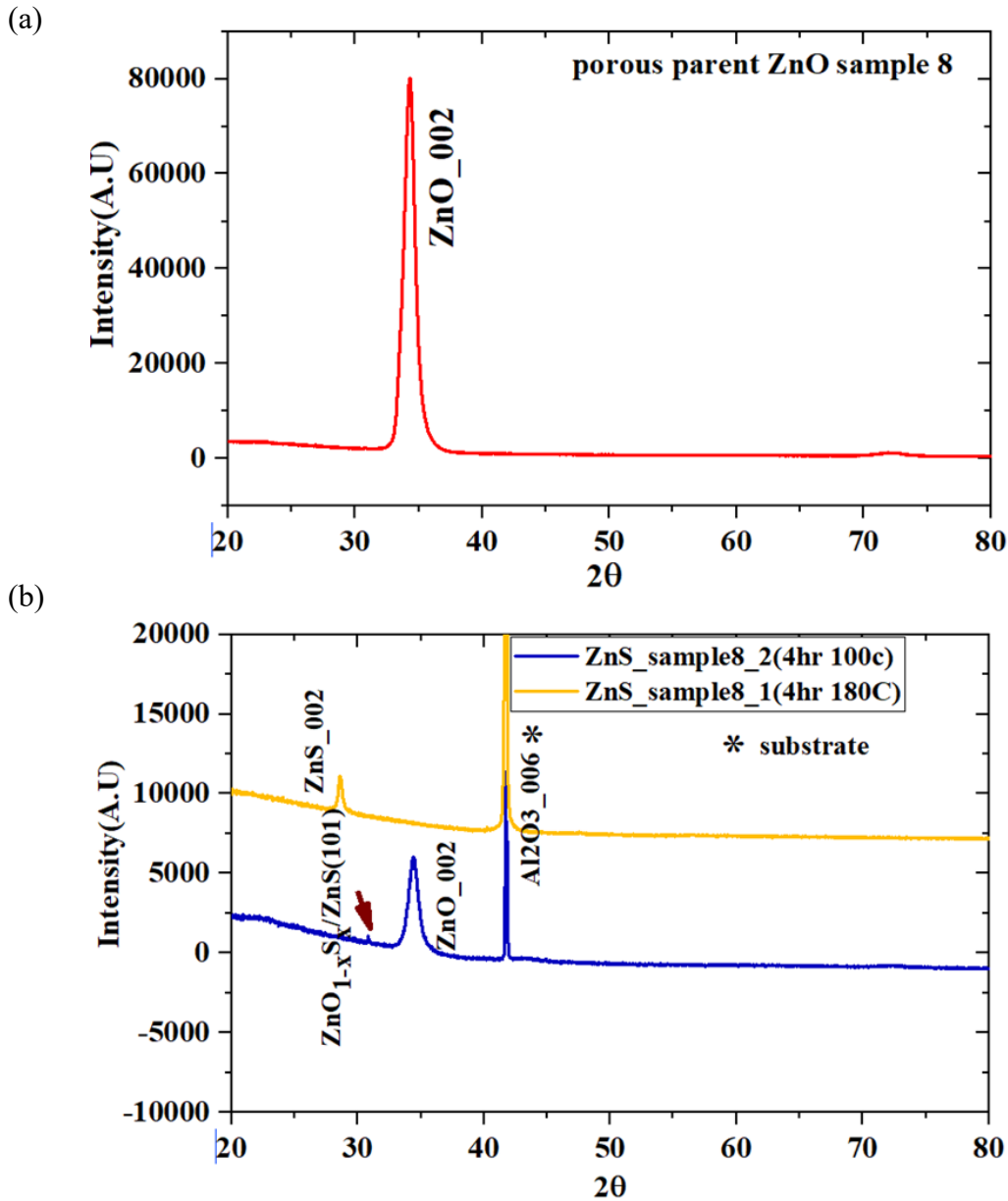
Figure 36: (a)XRD of a porous parent ZnO (b) Overlapping plot of 4 hours sulfidation at 180°C

However, the intensity of the peak corresponding to wurtzite ZnO (002) has significantly got reduced. Hence it can be deduced that activation energy of diffusion of S^{2-} ions is strongly dependent on temperature. More in depth analysis could be done on temperature dependence of activation energy of diffusion of anions and sulfidation kinetics. Additionally, the structural and optical properties can also be altered by varying the temperature of sulfidation.

Conclusions

ZnO-ZnS thin film heterostructures have been successfully synthesized by pulsed laser deposition and hydrothermal method where oxygen in the PLD grown ZnO thin films got replaced with sulfur by diffusion mechanism. XRD result shows partial and complete conversion from ZnO to ZnS thin film depending on the time of the sulfidation. Porosity and oxygen vacancy play important role in sulfidation process. In general, the more vacancy rich and porous the parent ZnO film, the more oxygen gets replaced by sulfur because sulfur atoms can easily migrate through vacancies. The crystallinity of the sulfidized films turn out poor compared to the parent films. Surface irregularities and uneven distribution of particles were clearly visible in the SEM pictures. The PL spectra of the ZnO films give information about the stoichiometry of the films and the defects that are present in the parent films. The optical band gap of the parent ZnO films turned out to be ~ 3.18ev which is less than the theoretical reported value 3.36ev. Blue emission band was observed in the porous ZnO films that were sulfidized for different amount of time. Sulfur vacancies are the plausible reason for blue emission of the sulfidized films as reported in some of the papers. From the Raman spectroscopy of the parent and the sulfidized films we could see the Raman active modes for wurtzite ZnO and ZnS structure. More analysis needs to be done through theoretical calculation and simulation to understand the temperature

and time dependency of diffusion mechanism which enables migration of sulfur atoms through

the crystal lattice for replacement of oxygen with sulfur in hydrothermal synthesis.

STRUCTURAL AND OPTICAL PROPERTIES OF ZnO-ZnS CORE-SHELL NANOPARTICLES HETEROSTRUCTURES

Abstract

Small ZnO nanoparticle is emerging as industry standard solid sorbent for removal of sulfur-based compound from fossil fuel. While sulfidation is limited to the surface of bulk ZnO, small ZnO nanoparticle is more effective for absorbing sulfur more efficiently. The structural and optical characteristics of sulfidized ZnO nanoparticle are studied in this paper. The wurtzite ZnO undergoes complete sulfidation to a new crystallographic structure comprised of mixed phase of sphalerite and wurtzite ZnS. The exchange of anion happens through diffusion process and contribute to substitutional doping. The sulfidized product nanoparticle had different size than the crystallite size of parent sample. The Photoluminescence spectra revealed more defect states within the band gap which is evident from the defect emission spectra in the visible region.

Introduction

ZnO nanoparticles have a wide range of applications such as energy storage, catalysis, coating and pigments, environmental remediation and many others.[40] ZnO has been used as a solid sorbent for removal of polluting sulfur from industrial petroleum-based fuel. Very few papers previously reported that sulfidation of ZnO bulk powder is limited to the surface whereas for the nano powder the entire ZnO can undergo complete sulfidation because of high sorbent capacity. ZnO nano powder can act as sorbent to scavenge sulfur compound such as hydrogen sulfide from petroleum-based products and fuels.[41] The reaction can be represented as

$ZnO+H_2S \rightarrow ZnS+H_2O$. The oxygen ions ($O^{2-}$) in the lattice get replaced by sulfur ions(S^{2-}). Specifically, for the nanoparticles, the more exposed surface area enables enhanced kinetics for sulfidation reaction at relatively low temperature. Banerjee and Jain reported much lower desulfurization temperature compared to conventional operating temperature in the range 650-800°C.[40] The mechanism of sulfidation process of nanoparticles has critical difference compared to the bulk material, even the few nm differences in size may have effect in sorbent design. In a study, Park *et al.*[42] reported sulfidation of hexagonal ZnO nano-particles of size 14 nm at 235°C using hexamethyldisilathiane. The reaction involved exchange of O^{2-} with S^{2-} in the crystal lattice. They also reported faster outward diffusion of Zn^{2+} compared to inward diffusion of S^{2-} which is known as nanoscale Kirkendall phenomenon which resulted hollow nanocrystalline structure. Another group of researchers reported growth of a protecting layer of ZnS on the surface of ZnO nanoparticle at relatively lower temperature. Where first stage of sulfidation reaction is relatively easy and rapid at low temperature, the bulk reaction is tough because of diffusion resistance.[15] Also, ZnO based sorbent can absorb more H_2S if large number of atoms are exposed on the surface. To increase sulfur intake by ZnO based sorbent at low temperature, complete sulfidation of bulk ZnO is required. For this complete sulfidation, diffusion through primary ZnS layer must be accelerated. However, very less detailed information is available about the sulfidation kinetics. Till this date it has been established that inward growth leads to formation of ZnS layer where sulfur diffuses from external ZnS/H_2S layer to the ZnS/ZnO interface and oxygen atoms which are transferred to inverse direction can be combined to the proton and resulted in water molecules.[15] However, new data has also emerged which has shown sulfidation of ZnO nanorods with H2S in liquid medium. It has shown Kirkendall effect which resulted in outward growth of ZnS layer. In this process, diffusion of Zn^{2+} and O^{2-} happens

through ZnS layer to the external ZnS/H$_2$S interface. Zn^{2+} cation combine with sulfur and O^{2-} combines with protons to result in H$_2$O molecules. The figure 37 represents schematic of ZnS growth during sulfidation of ZnO.
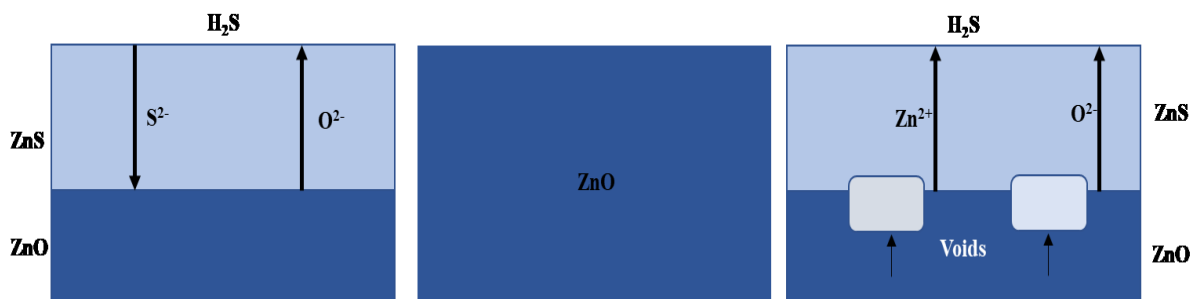
Figure 37: Mechanism of ZnS growth during ZnO sulfidation of inward and outward growth

In my experiment, I have studied the sulfidation of ZnO nanoparticles for 16 hours ,6 hours and 1 hour using X-ray crystallography and optical spectroscopy. Structural and optical characteristics were analyzed before and after sulfidation.

Experimental Methods

ZnO-ZnS CSNPs have been synthesized using hydrothermal synthesis. 200mg thiourea mixed with 40ml DI water served as precursor solution. 60 mg of ZnO nano powder was well dispersed in 0.066 M thiourea solution by means of probe sonicator and sulfidized for 16 hours, 6 hours and 1 hour, respectively at 180°C in an autoclave. After sulfidation, the autoclave was cooled down to the room temperature and sulfidized samples were recovered by centrifugation. The phase and crystallinity of the sulfidized samples were characterized by x- ray diffractometer (Bruker AXS D8) equipped with high-resolution detector using Cu-Kα source with wavelength

of 1.5406Å. The operating voltage and current were 40 KV and 40 mA respectively. θ-2θ scan was performed from 20° to 80° after optimization of ϕ and Z axis scan. The data were analyzed using Origin pro 8.5. Surface morphology and elemental analysis of the sulfidized heterostructures were done using scanning electron microscopy (Fei Quanta 2000) and energy dispersive x-ray spectroscopy (EDS) that has been equipped with in the scanning electron microscope.

Raman spectroscopy was conducted on both as grown and sulfidized nanoparticle to study the vibrational modes present in the system. The As-grown ZnO and sulfidized samples were characterized using 532nm green laser by Horiba Labram HR Raman PL system.

PL spectroscopy was also conducted where the samples were irradiated with 325 nm, He-Cd laser source at room temperature. Excitation energy was above the band gap of the material. The samples were flattened on a metal bar of tungsten carbide which contributes minimum background signal. The 15x NUV-lens was used for focusing on the localized spot and measurements were taken at multiple spots. Beam splitter UV splits the scattered light from the samples according to the wavelength. The scan was taken in the range of 350-750 nm while acquisition time was 20 seconds, and 20 scans were taken in average in that wavelength range. Both Raman and PL spectroscopy data were analyzed using Origin pro 8.5 software.

Results and Discussion

Figure 38 represents the XRD pattern of the wurtzite ZnO nano powder which reveals that the sample was polycrystalline in nature. Figure 39 represents the cif file of wurtzite ZnO which matches with the experimental values. From the XRD data of the ZnO wurtzite sample I

can conclude that the sample was polycrystalline in nature which was not preferentially oriented as opposed to the thin films. Lattice parameters of the ZnO nanoparticles found out to be consistent with the theoretical value. Table 10 represents the lattice parameters of wurtzite ZnO which are consistent with the theoretical value.
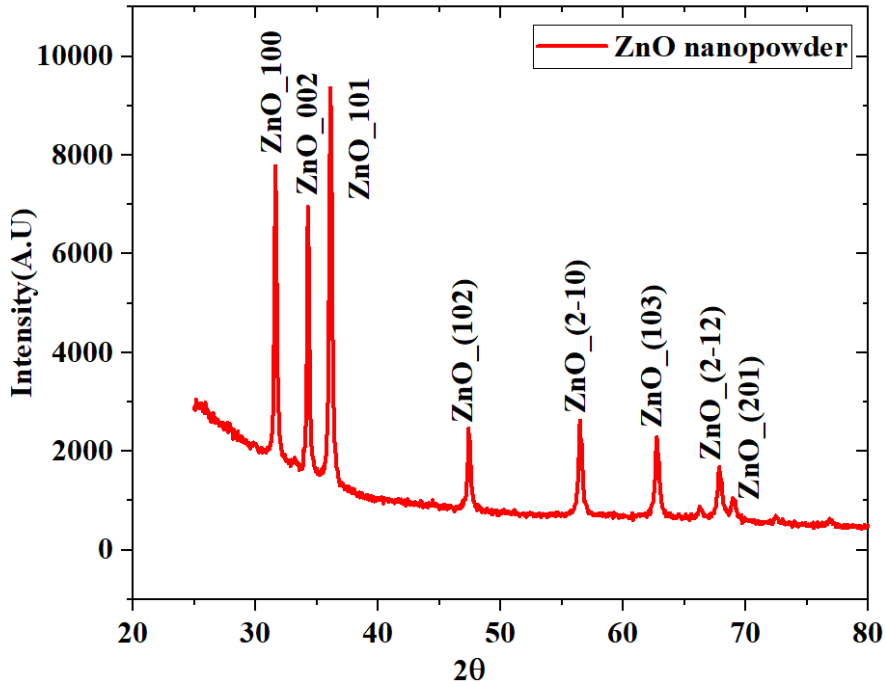
Figure 38: XRD of wurtzite ZnO nano powder

Table 10: Lattice parameters of wurtzite ZnO

2θ (°)	dhkl	h k l	a(Å)	c(Å)
31.67	2.8229	1 0 0	3.259	5.321
34.3	2.612	0 0 2	3.199	5.224
36.11	2.485	1 0 1	3.244	5.298
47.358	1.918	1 0 2	3.227	5.271
56.45	1.628	2 -1 0	3.25	5.307

The values of the average lattice parameters were calculated as a = 3.23Å and c = 5.28Å.
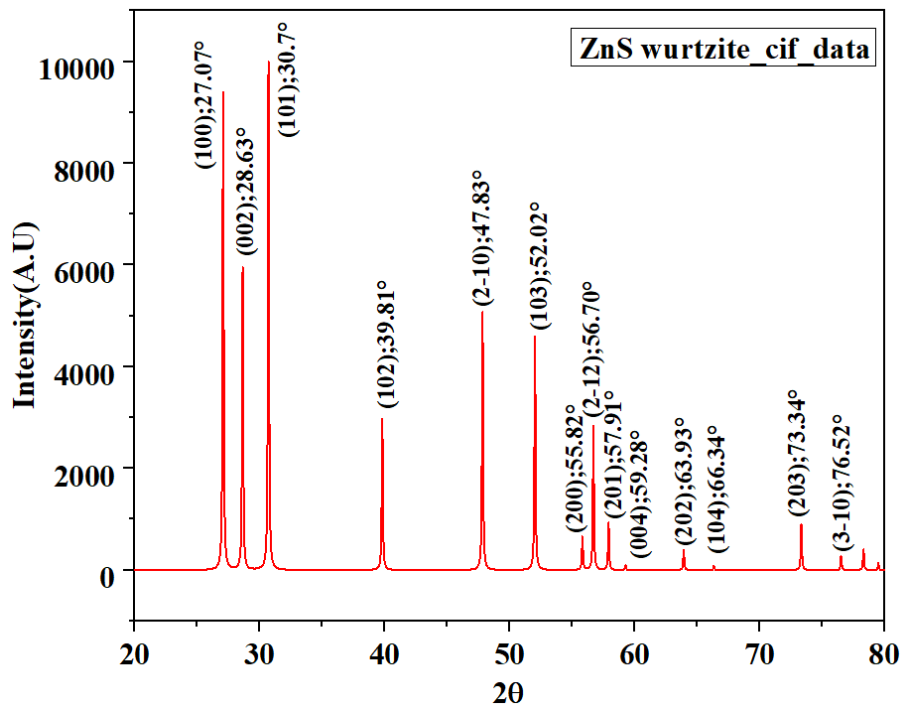
Figure 39: Cif data of wurtzite ZnS

Figure 40 shows XRD plot of the ZnS nano powder which is sulfidized for 16 hours. From the XRD plot of the ZnS nanoparticles sulfidized by hydrothermal synthesis for 16 hours, wurtzite ZnO nanoparticles have been converted to ZnS nanoparticles comprising of mixed phase of wurtzite and sphalerite structures. This is supported by the complete loss of diffraction peaks of wurtzite ZnO and appearance of diffraction peaks corresponding to (002) plane of wurtzite ZnS and (200) plane of sphalerite ZnS and other peaks of mixed phases as mentioned in the figure. Although researchers Ma *et al.*[41] reported formation of sphalerite phase than formation of the mixed phase as in case of our experiment.
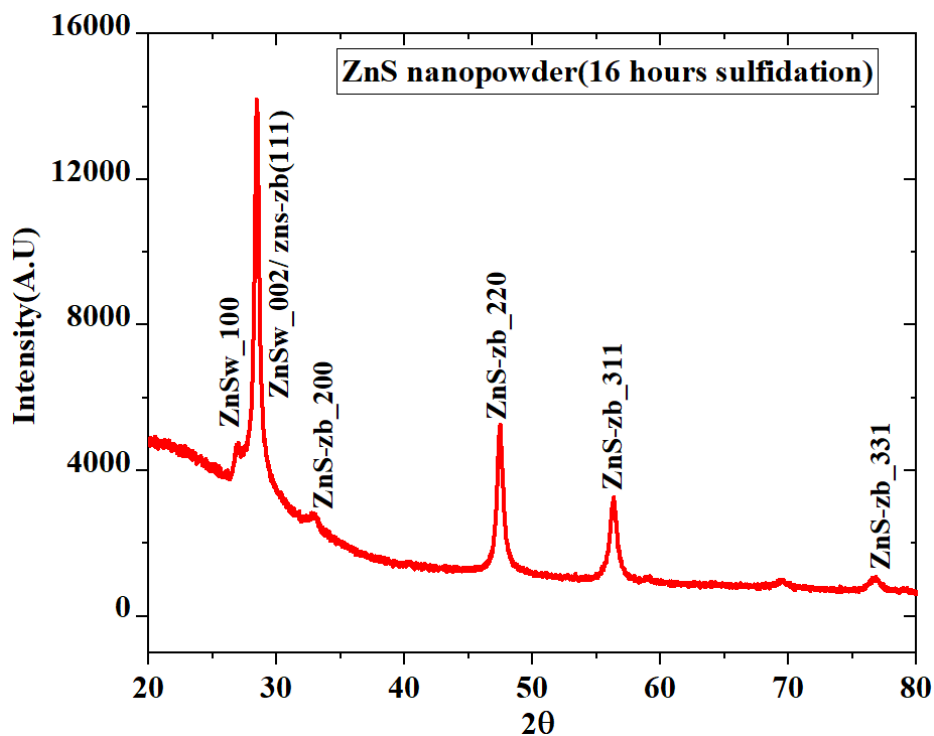
Figure 40: XRD of ZnS nano powder sulfidized for 16 hours

The inter planar spacing corresponding to 2θ ~ 28.5° turned out to be 3.129 Å which is very

close to the reported value for zinc-blende phase. Although, some researchers reported formation

of the mixed phase of wurtzite and sphalerite phases.[15] The particle size of synthesized ZnS

nanoparticles can be calculated using Debye-Scherrer equation. The XRD plots of the 6 hours

and 1-hour sulfidation are represented below in Figures 41 and 42, respectively. These plots are

consistent with the plot of 16 hours sulfidized ZnO NPs. From the XRD plots of sulfidized NPs it

was observed that the positions of the diffraction peaks of the sulfidized nanoparticles for

different times were very little different although the intensities were comparatively low for 6

hours and 1 hour sulfidized nanoparticles than the 16 hours sulfidized one. Also, omission of the

wurtzite (100) phase and sphalerite (200) phase in 1 hour sulfidized nanoparticle were evident.

Further investigation is needed in order to study the sulfidation kinetics for varying amount of

time for ZnO nanoparticles.
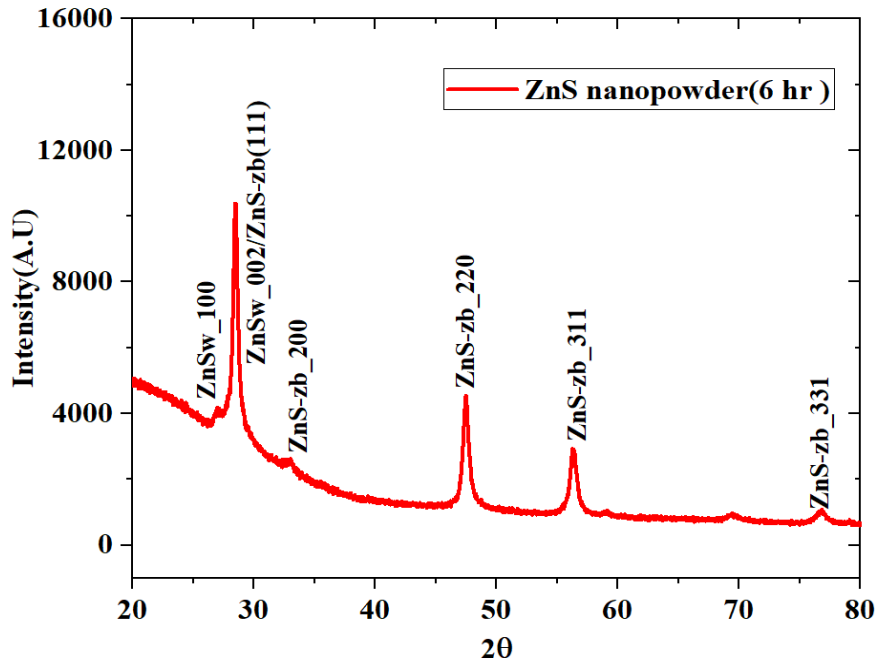
Figure 41: XRD of ZnS nano powder (6 hours sulfidized)
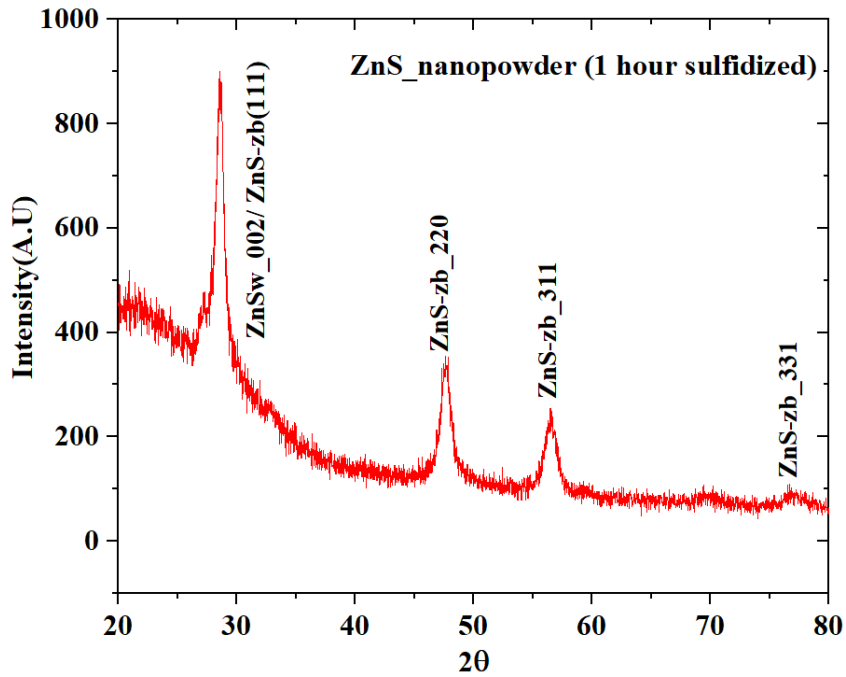
Figure 42: XRD of ZnS nano powder (1 hour sulfidized)

Figure 43 shows the overlapping plot of the sulfidized nanoparticles for different hours.
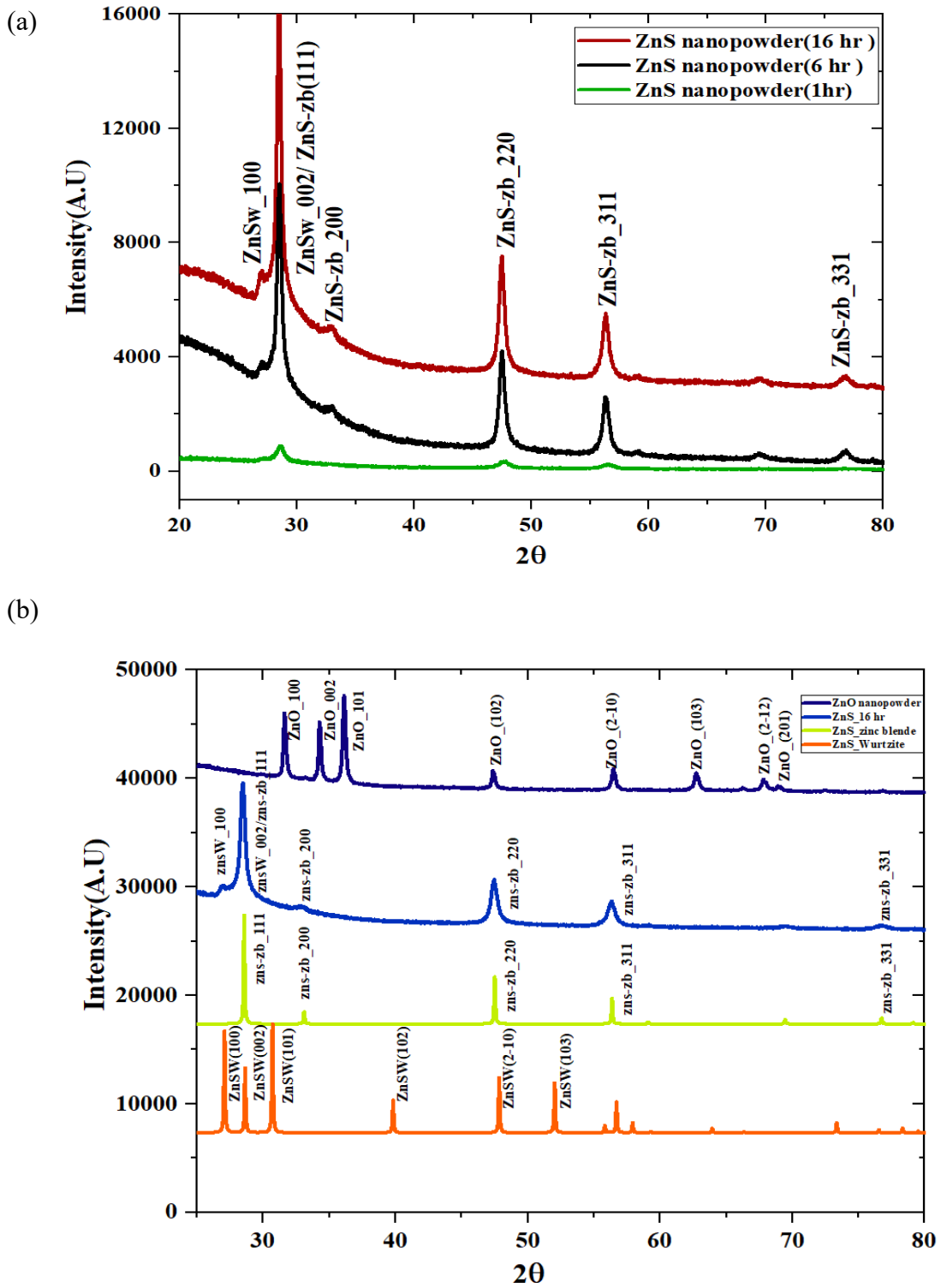
Figure 43: a) Overlapping XRD plot of ZnO nano powders sulfidized for different hours b) comparison with ZnS cif data

SEM and EDS were performed on the sulfidized nanoparticles. Figure 44 represents SEM micrograph of pure ZnO and sulfidized NPs of 16 hours and 6 hours, respectively. From the SEM micrograph of pure ZnO NP, clustered and cloudy particles were observed. The 1 hour sulfidized picture is also quite clustered. Distinct particles are almost invisible.
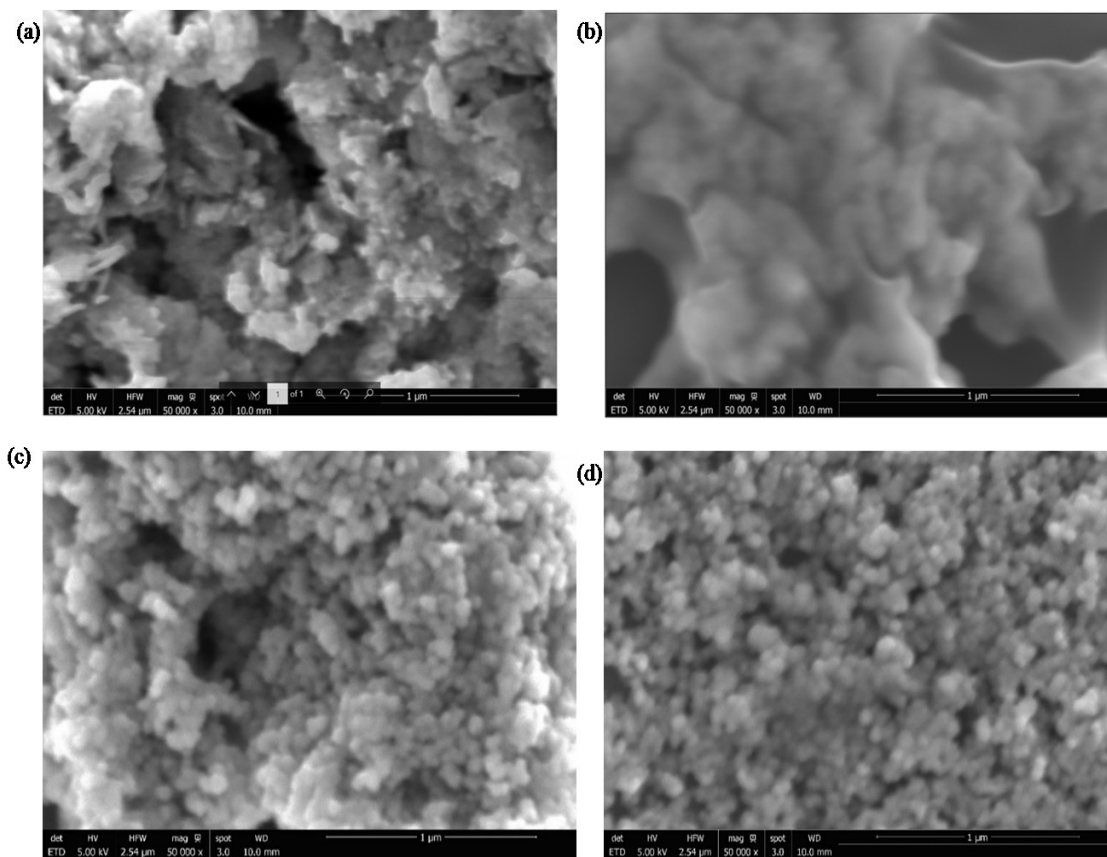
Figure 44: SEM micrographs of (a) pure ZnO nanoparticles (b) ZnS nanoparticles (1 hour sulfidized), (c) 6 hours, and (d) 16 hours

From the SEM picture of ZnO nanoparticle, I observed cloudy and blurry crystals of ZnO. Researchers have reported this kind of micrograph due to presence of hydroxyl group of ions present in aqueous solution of ZnO. This holds true for the sulfidized NPs of 1 hour. This must have been very small amount of time for the nanoparticles to be free of the hydroxyl ions.

Additionally, smaller particle size for 16 hours sulfidized nanoparticles compared to the 6 hours sulfidized one can be seen. Some researchers reported the smaller the particle size the more sulfidation will take place. Further, formation of cavities or voids within the structure were also observed. This might have happened due to outward growth of ZnS followed by the diffusion of Zn^{2+} and O^{2-} ions to the external interface of ZnS/H$_2$S(liquid) as known as Kirkendall effect.[15]Also, the 6 hours sulfidized nanoparticle seems to be appeared more clustered. Rouhi *et al.*[43] reported in their paper that voids have been formed at the ZnO- ZnS interface for partially sulfidized ZnO. According to the paper the paper the voids formed due to zinc and oxygen vacancies in ZnO which coalesce together and aid the formation of voids at the interface of ZnO and ZnS. As the interface between ZnO and ZnS phase is reduced it limits the diffusion of zinc and oxygen into ZnS phase. Diffusion of zinc and oxygen atoms are very important for sulfidation reaction which has direct impact on sulfidation kinetics.[43] The EDS spectra gives the information about the compositions of the constituent elements. Figure 45 shows the constitutional analysis of the 16 hours and 6 hours sulfidized nanoparticles respectively.
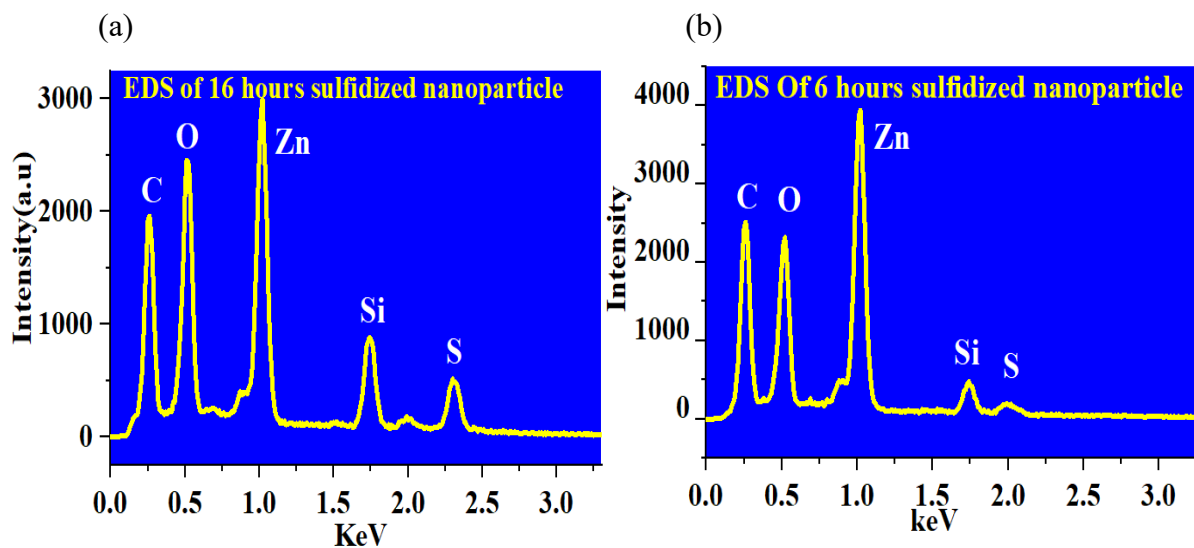

Figure 45: EDS analysis of sulfidized NPs for (a) 16 hours and (b) 6 hours

The Raman spectra of the sulfidized CSNPs have been studied. Figure 46 shows the Raman active modes of 1 hour ,6 hours and 16 hours sulfidized ZnO NPS.
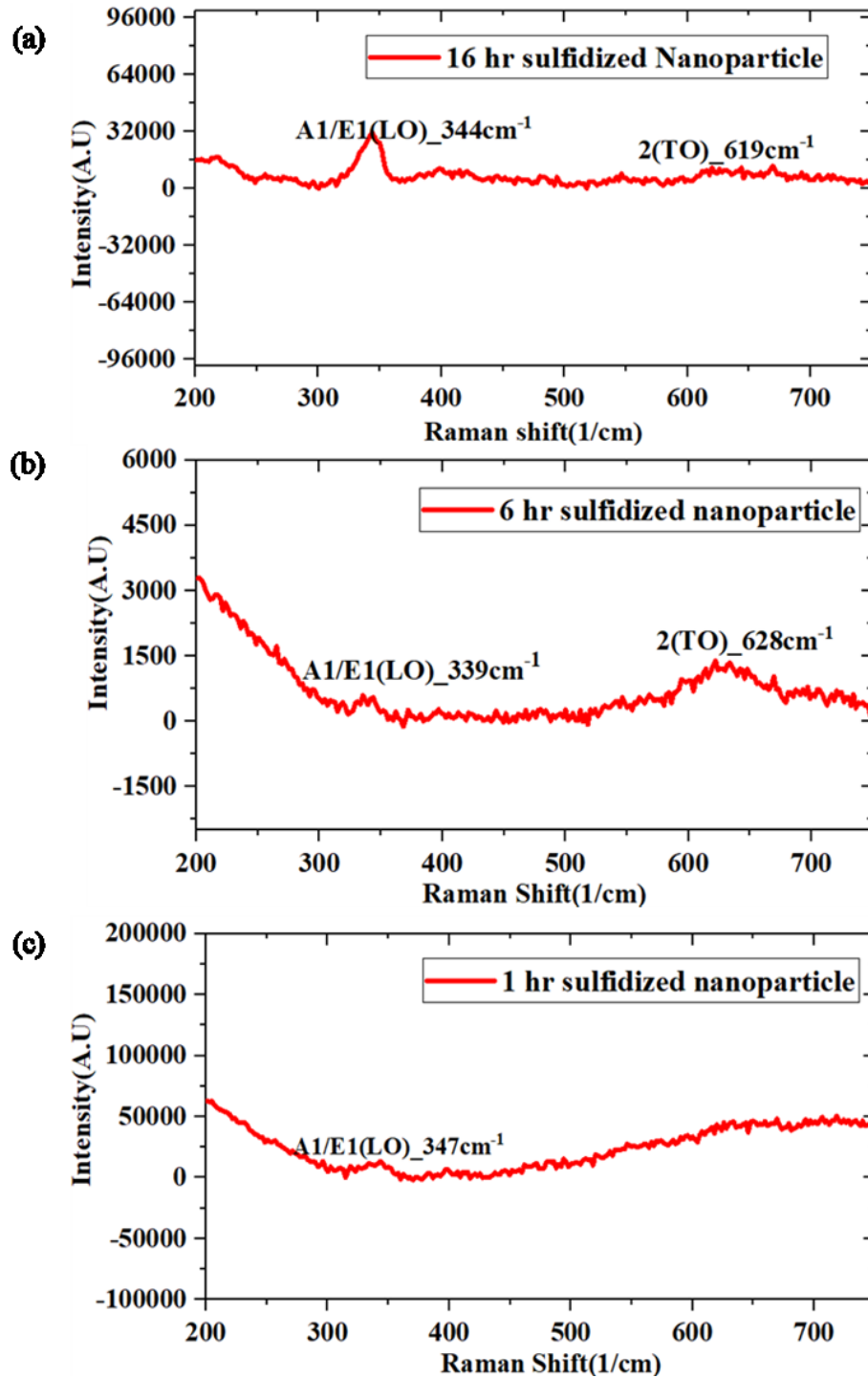

Figure 46: Raman active modes of sulfidized NPs for (a)16 hours, (b) 6 hours, and (c) 1 hour

From these spectra fewer number of Raman active modes compared to the sulfidized thin films were observed. A first order scattering around 344 cm^{-1} related to A1 and E1 symmetry mode was observed for all sulfidized NPs. However, for the sulfidized thin film samples this mode appeared around 347 cm^{-1}. Brafman and Mitra reported this mode at 351 cm^{-1} while other group of researchers observed this mode around 352 cm^{-1} at room temperature.[28,29] A second order Raman active mode was observed 619 cm^{-1} for 16 hours and 6 hours sulfidized NPs. Cheng *et al.*[32] reported 2nd order TO mode around 622 cm^{-1}. However, this mode was not observed for 1 hour sulfidized NPs. Therefore, it can be concluded that after significant amount of time during the sulfidation 2nd order TO mode can be observed. More research needs to be conducted to understand the omission of the Raman active modes of sulfidized NPs compared to the sulfidized thin films.

To investigate the optical properties of the ZnO-ZnS core shell nanoparticles, PL spectroscopy was performed at room temperature. Figures 47 and 48 represent the PL spectra of the ZnO-ZnS CSNPs sulfidized for 16 hours and ZnO nanoparticles for reference. The samples were excited using 325 nm He-Cd laser. Several researchers have reported blue emission of ZnS nanoparticles under UV excitation at 428 nm. Becker and Bard attributed this blue emission due to the sulfur (S^{2-}) vacancies.[36] Murase *et al.*[44] suggested blue emission band around 470 nm to Zn^{2+} acceptor ions. Yanagida *et al.*[45] have reported defect related emission at 420 nm. Although in our experiment no peak is visible around 428nm related to excitonic emission as opposed to ZnO-ZnS thin films. In ZnO-ZnS NP heterostructure, PL spectra appear at significant lower energy level than the theoretical optical band gap energy (3.54ev for ZB and 3.91ev for Wurtzite ZnS). This supports favorable transition from energy states inside the band gap. Chen *et al.*[46] attributed PL peaks at the lower energy level than the band gap to the surface states. According

to the author, as the particle size decreases, the surface to volume ratio and surface states increase. It was also proved by their thermo-luminescence measurement.
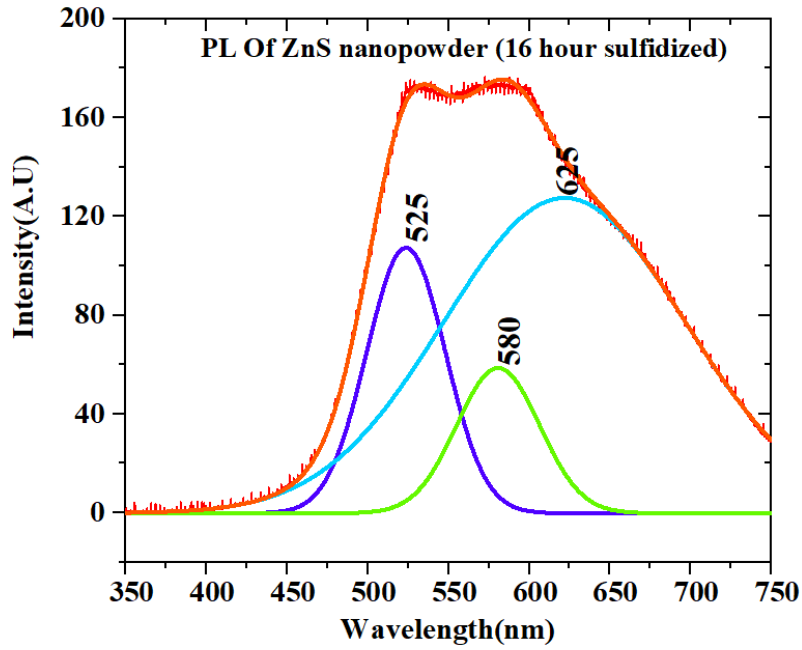
Figure 47: PL spectra of 16 hours sulfidized nanoparticles
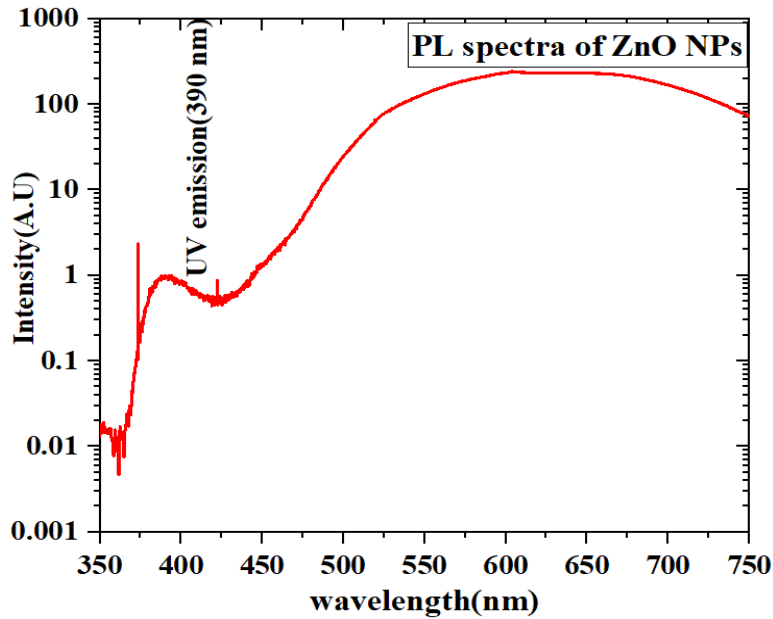
Figure 48: PL spectra of ZnO NP

As a result, the probability of excitonic recombination decreases via non-radiative surface states recombination. So, the defect emission peaks around~ 525, 583 and 625 nm might have resulted from prevalence of surface defect states present in the ZnO sample that is sulfidized for 16 hours. Figure 49 shows defect states of ZnS NP. Figures 50 and 51 represent plots of PL of ZnO sample that are sulfidized for 6 hours and 1 hour.
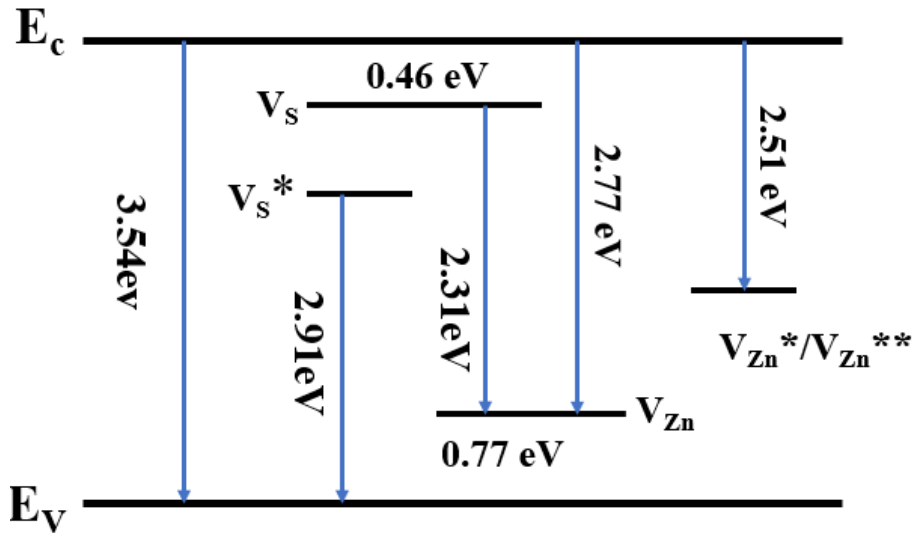
Figure 49: Defect emission states of ZnS ZB

In the literature PL peaks ~ 2.90ev/2.91ev is assigned to singly ionized sulfur vacancies.[47] The emissions ~ 2.76/2.77ev are ascribed to Zn vacancies. Further researchers reported spectra ~ 2.31ev due to emission from the sulfur vacancies to Zn vacancies.[47] The emission spectra of 6 hours and 1 hour sulfidized ZnO NPs are consistent with the result of 16 hours sulfidation. These plots also suggested PL emission peaks around ~ 2.36ev, 2.13ev and 2ev. So, in my experiment the emission spectra ~ 2.36ev might have resulted from transition to Zn vacancies from sulfur vacancies.

Also as suggested from the XRD data of the ZnO-ZnS NP heterostructure, majority of the ZnO was converted to ZnS preferably with sphalerite structure, more time and temperature-controlled synthesis needs to be done in order to understand sulfidation kinetics and defect emission of the heterostructure.
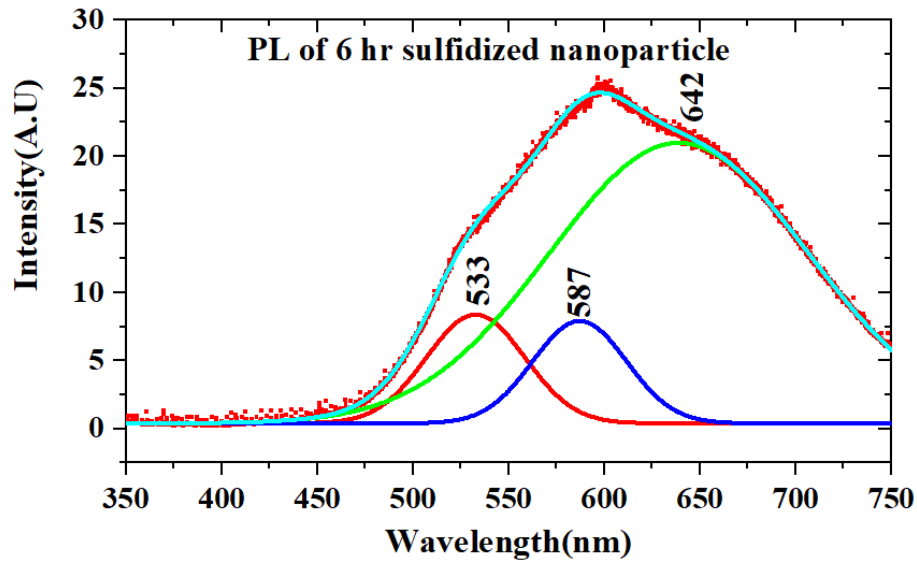
Figure 50: PL of ZnS nanoparticles (6 hours sulfidized)
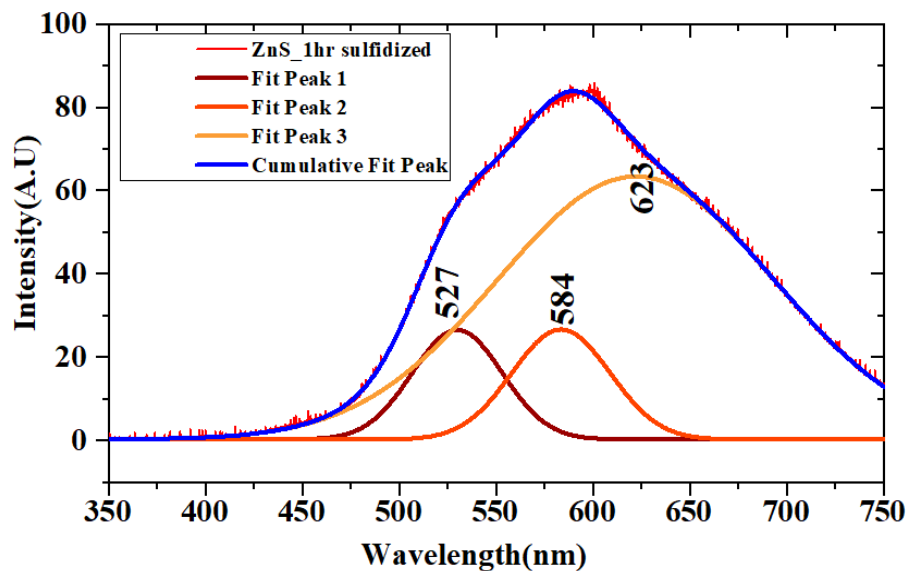
Figure 51: PL of ZnS nanoparticles (1 hour sulfidized)

Conclusions

ZnO-ZnS core-shell nanoparticles had been successfully formed due to sulfidation of ZnO nanoparticles at 180°C for varying amount of time. At 180°C voids might have formed at ZnO-ZnS interface which facilitated ZnS nanoparticle formation. Previous researchers have reported this kind of growth during sulfidation of ZnO nanorods.[48] This is evidence of Kirkendall effect which suggests outward growth of ZnS layer. Several studies have shown that while reaction has been carried out between ZnO and H_2S at 350°C, voids still formed after partial transformation, but are absent for completely transformed ZnS. Other researchers reported sulfidation of ZnO nanoparticles where O^{2-} ions are substituted by S^{2-} ions.[48] Mixed phase of ZnS wurtzite and zinc-blende formed during the sulfidation process. The more S^{2-} are available more ZnS domains grow combining with Zn^{2+} ions.[48] From the XRD analysis we confirm that initial wurtzite structure of ZnO is not retained after nucleation-growth process of forming ZnS. It has also been found that the difference between the unit cell of ZnO and ZnS induces lattice strain. The PL spectra confirm prevalence of defect states inside the band gap which gives rise to emission in the visible region.

CONCLUSIONS

Sulfur doped heterostructures of ZnO-ZnS have been successfully synthesized at 180°C using PLD and hydrothermal synthesis where oxygen is exchanged with sulfur for both the thin film and nanoparticles. Structural characterization has been performed using XRD and SEM which indicate the partial to complete exchange of oxygen ion with sulfur ion in ZnO through hydrothermal method. It also shows that oxygen vacancies play an important role in the sulfidation process. ZnS might have grown through void formation at the ZnO-ZnS interface. For the thin film we have seen that initial wurtzite crystal structure of the thin film has retained and an intermediate phase known as zinc-oxysulfide might have grown after sulfidation where for the nanoparticles, a mixed phase of sphalerite and wurtzite ZnS has formed after sulfidation. From the Raman spectroscopy one can observe the Raman active modes of ZnO and ZnS, though further investigation is needed for determination of the Raman active modes of $ZnO_{1-x}S_x$. PL spectra of the pure and sulfidized thin films and the nanoparticles has provided information about the defect states which causes electronic transition in the visible region. PL spectra also helped us find the band gap of the ZnO-ZnS heterostructures. Researchers have observed ferromagnetism of non-stoichiometric ZnS microspheres. Therefore, along with optoelectronic applications, the ZnO-ZnS thin film/ core-shell nano- heterostructure can be exploited to study novel ferromagnetic behavior in future.

REFERENCES

1   G. Bastard, *Wave mechanics applied to semiconductor heterostructures*, 1990.

2   M. Jaros, *Wave Mechanics Applied to Semiconductor Heterostructures*, Taylor & Francis, 1991.

3   M.-Y. Lu, J. Song, M.-P. Lu, C.-Y. Lee, L.-J. Chen and Z. L. Wang, ZnO−ZnS Heterojunction and ZnS Nanowire Arrays for Electricity Generation, *ACS Nano*, 2009, **3**(2), 357–362.

4   R. Dingle, H. L. Störmer, A. C. Gossard and W. Wiegmann, Electron mobilities in modulation-doped semiconductor heterojunction superlattices, *Appl. Phys. Lett.*, 1978, **33**(7), 665–667.

5   L. J. Lauhon, M. S. Gudiksen and C. M. Lieber, Semiconductor nanowire heterostructures, *Philos. Trans. R. Soc. London. Ser. A Math. Phys. Eng. Sci.*, 2004, **362**(1819), 1247–1260.

6   S. R. White and L. J. Sham, Electronic Properties of Flat-Band Semiconductor Heterostructures, *Phys. Rev. Lett.*, 1981, **47**(12), 879–882.

7   V. I. Tolstikhin, Optical properties of semiconductor heterostructures for active photonic device modeling, *J. Vac. Sci. Technol. A Vacuum, Surfaces, Film.*, 2000, **18**(2), 605–609.

8   J. Yan, X. Fang, L. Zhang, Y. Bando, U. K. Gautam, B. Dierre, T. Sekiguchi and D. Golberg, Structure and Cathodoluminescence of Individual ZnS/ZnO Biaxial Nanobelt Heterostructures, *Nano Lett.*, 2008, **8**(9), 2794–2799.

9   W. Tian, C. Zhang, T. Zhai, S.-L. Li, X. Wang, J. Liu, X. Jie, D. Liu, M. Liao, Y. Koide, D. Golberg and Y. Bando, Flexible Ultraviolet Photodetectors with Broad Photoresponse Based on Branched ZnS-ZnO Heterostructure Nanofilms, *Adv. Mater.*, 2014, **26**(19), 3088–3093.

10   E. Y. Muslih and B. Munir, in *Emerging Solar Energy Materials*, InTech, 2018.

11   H. Morkoç and Ü. Özgür, *Zinc oxide: fundamentals, materials and device technology*, John Wiley & Sons, 2008.

12   J. Cheng, D. Fan, H. Wang, B. Liu, Y. Zhang and H. Yan, Chemical bath deposition of crystalline ZnS thin films, *Semicond. Sci. Technol.*, 2003, **18**(7), 676–679.

13   L. Qi, G. Mao and J. Ao, Chemical bath-deposited ZnS thin films: Preparation and characterization, *Appl. Surf. Sci.*, 2008, **254**(18), 5711–5714.

14   R. Zhang, B. Wang and L. Wei, Influence of RF power on the structure of ZnS thin films grown by sulfurizing RF sputter deposited ZnO, *Mater. Chem. Phys.*, 2008, **112**(2), 557–

561.

15 I. Bezverkhyy, J. Skrzypski, O. Safonova and J.-P. Bellat, Sulfidation Mechanism of Pure and Cu-Doped ZnO Nanoparticles at Moderate Temperature: TEM and In Situ XRD Studies, *J. Phys. Chem. C*, 2012, **116**(27), 14423–14430.

16 D. Lehr, M. Luka, M. R. Wagner, M. Bügler, A. Hoffmann and S. Polarz, Band-gap engineering of zinc oxide colloids via lattice substitution with sulfur leading to materials with advanced properties for optical applications like full inorganic UV protection, *Chem. Mater.*, 2012, **24**(10), 1771–1778.

17 S. Kar and S. Chaudhuri, Controlled Synthesis and Photoluminescence Properties of ZnS Nanowires and Nanoribbons, *J. Phys. Chem. B*, 2005, **109**(8), 3298–3302.

18 F. Göde, Annealing temperature effect on the structural, optical and electrical properties of ZnS thin films, *Phys. B Condens. Matter*, 2011, **406**(9), 1653–1659.

19 M. Salah, S. Azizi, A. Boukhachem, C. Khaldi, M. Amlouk and J. Lamloumi, in *2016 7th International Renewable Energy Congress (IREC)*, IEEE, 2016, pp. 1–5.

20 L. Cui, H. Y. Zhang, G. G. Wang, F. X. Yang, X. P. Kuang, R. Sun and J. C. Han, Effect of annealing temperature and annealing atmosphere on the structure and optical properties of ZnO thin films on sapphire (0 0 0 1) substrates by magnetron sputtering, *Appl. Surf. Sci.*, 2012, **258**(7), 2479–2485.

21 R. Zhang, P.-G. Yin, N. Wang and L. Guo, Photoluminescence and Raman scattering of ZnO nanorods, *Solid State Sci.*, 2009, **11**(4), 865–869.

22 Y. Kavanagh and D. . Cameron, Zinc sulfide thin films produced by sulfidation of sol–gel deposited zinc oxide, *Thin Solid Films*, 2001, **398**–**399**, 24–28.

23 R. Zhang, B. Wang and L. Wei, Sulfidation growth and characterization of nanocrystalline ZnS thin films, *Vacuum*, 2008, **82**(11), 1208–1211.

24 M. Laurenti and V. Cauda, Porous Zinc Oxide Thin Films: Synthesis Approaches and Applications, *Coatings*, 2018, **8**(2), 67.

25 M. Koyano, P. QuocBao, L. T. ThanhBinh, L. HongHa, N. NgocLong and S. Katayama, Photoluminescence and Raman Spectra of ZnO Thin Films by Charged Liquid Cluster Beam Technique, *Phys. status solidi*, 2002, **193**(1), 125–131.

26 X. Q. Wei, B. Y. Man, M. Liu, C. S. Xue, H. Z. Zhuang and C. Yang, Blue luminescent centers and microstructural evaluation by XPS and Raman in ZnO thin films annealed in vacuum, N2 and O2, *Phys. B Condens. Matter*, 2007, **388**(1–2), 145–152.

27 Q. Xiong, J. Wang, O. Reese, L. C. Lew Yan Voon and P. C. Eklund, Raman Scattering

from Surface Phonons in Rectangular Cross-sectional w-ZnS Nanowires, *Nano Lett.*, 2004, **4**(10), 1991–1996.

28   O. Brafman and S. S. Mitra, Raman Effect in Wurtzite- and Zinc-Blende-Type ZnS Single Crystals, *Phys. Rev.*, 1968, **171**(3), 931–934.

29   C. A. Arguello, D. L. Rousseau and S. P. S. Porto, First-Order Raman Effect in Wurtzite-Type Crystals, *Phys. Rev.*, 1969, **181**(3), 1351–1363.

30   J. Schneider and R. D. Kirby, Raman Scattering from ZnS Polytypes, *Phys. Rev. B*, 1972, **6**(4), 1290–1294.

31   Y. Ebisuzaki and M. Nicol, Raman spectrum of hexagonal zinc sulfide at high pressures, *J. Phys. Chem. Solids*, 1972, **33**(3), 763–766.

32   Y. C. Cheng, C. Q. Jin, F. Gao, X. L. Wu, W. Zhong, S. H. Li and P. K. Chu, Raman scattering study of zinc blende and wurtzite ZnS, *J. Appl. Phys.*, 2009, **106**(12), 123505.

33   H. Zeng, G. Duan, Y. Li, S. Yang, X. Xu and W. Cai, Blue Luminescence of ZnO Nanoparticles Based on Non-Equilibrium Processes: Defect Origins and Emission Controls, *Adv. Funct. Mater.*, 2010, **20**(4), 561–572.

34   W. Zhaoyang and H. Lizhong, Effect of oxygen pressure on the structural and optical properties of ZnO thin films on Si (111) by PLD, *Vacuum*, 2009, **83**(5), 906–909.

35   B. J. Jin, S. H. Bae, S. Y. Lee and S. Im, Effects of native defects on optical and electrical properties of ZnO prepared by pulsed laser deposition, *Mater. Sci. Eng. B*, 2000, **71**(1–3), 301–305.

36   W. G. Becker and A. J. Bard, Photoluminescence and photoinduced oxygen adsorption of colloidal zinc sulfide dispersions, *J. Phys. Chem.*, 1983, **87**(24), 4888–4893.

37   D. Denzler, M. Olschewski and K. Sattler, Luminescence studies of localized gap states in colloidal ZnS nanocrystals, *J. Appl. Phys.*, 1998, **84**(5), 2841–2845.

38   P. Hu, Y. Liu, L. Fu, L. Cao and D. Zhu, Self-Assembled Growth of ZnS Nanobelt Networks, *J. Phys. Chem. B*, 2004, **108**(3), 936–938.

39   B. Bhattacharjee and C.-H. Lu, Multicolor luminescence of undoped zinc sulfide nanocrystalline thin films at room temperature, *Thin Solid Films*, 2006, **514**(1–2), 132–137.

40   P. Banerjee and P. K. Jain, Mechanism of sulfidation of small zinc oxide nanoparticles, *RSC Adv.*, 2018, **8**(60), 34476–34482.

41   R. Ma, C. Levard, F. M. Michel, G. E. Brown and G. V. Lowry, Sulfidation Mechanism

for Zinc Oxide Nanoparticles and the Effect of Sulfidation on Their Solubility, *Environ. Sci. Technol.*, 2013, **47**(6), 2527–2534.

42   J. Park, H. Zheng, Y. Jun and A. P. Alivisatos, Hetero-Epitaxial Anion Exchange Yields Single-Crystalline Hollow Nanoparticles, *J. Am. Chem. Soc.*, 2009, **131**(39), 13943–13945.

43   J. Rouhi, C. H. R. Ooi, S. Mahmud and M. R. Mahmood, Synthesis of needle-shape ZnO-ZnS core-shell heterostructures and their optical and field emission properties, *Electron. Mater. Lett.*, 2015, **11**(6), 957–963.

44   N. Murase, R. Jagannathan, Y. Kanematsu, M. Watanabe, A. Kurita, K. Hirata, T. Yazawa and T. Kushida, Fluorescence and EPR characteristics of Mn2+-doped ZnS nanocrystals prepared by aqueous colloidal method, *J. Phys. Chem. B*, 1999, **103**(5), 754–760.

45   S. Yanagida, H. Kawakami, K. Hashimoto, T. Sakata, C. Pac and H. Sakurai, Photocatalysis of zinc sulfide microcrystals in reductive hydrogen evolution in water/methanol systems, *Chem. Lett.*, 1984, **13**(8), 1449–1452.

46   W. Chen, Z. Wang, Z. Lin and L. Lin, Absorption and luminescence of the surface states in ZnS nanoparticles, *J. Appl. Phys.*, 1997, **82**(6), 3111–3115.

47   J. Dong, X. Zeng, W. Xia, X. Zhang, M. Zhou and C. Wang, Ferromagnetic behavior of non-stoichiometric ZnS microspheres with a nanoplate-netted surface, *RSC Adv.*, 2017, **7**(34), 20874–20881.

48   L. Neveux, D. Chiche, D. Bazer-Bachi, L. Favergeon and M. Pijolat, New insight on the ZnO sulfidation reaction: Evidences for an outward growth process of the ZnS phase, *Chem. Eng. J.*, 2012, **181**–**182**, 508–515.